

# Chapter 2

## Catastrophic Slide: Vaiont Landslide, Italy

---

### TABLE OF CONTENTS

- 2.1 The Landslide ..... 34
- 2.2 Geological Setting ..... 39
- 2.3 The Sliding Surface ..... 42
- 2.4 Monitoring Data Before the Slide..... 44
- 2.5 Water Pressures and Rainfall..... 45
- 2.6 A Simple Stability Model..... 47
  - 2.6.1 Kinematics of the slide..... 48
  - 2.6.2 Two-block model..... 50
  - 2.6.3 Two interacting wedges ..... 54
  - 2.6.4 Static equilibrium at failure..... 61
  - 2.6.5 Safety factors ..... 64
  - 2.6.6 Landslide run out ..... 68
- 2.7 Discussion ..... 72
- 2.8 Lessons Learned ..... 73
  - 2.8.1 Slide reactivation ..... 73
  - 2.8.2 Submerging the slide toe..... 73
  - 2.8.3 Interpretation of field data..... 75
  - 2.8.4 Computational procedures ..... 76
  - 2.8.5 Could it have been avoided? ..... 77
- Appendix 2.1 Safety Factor  $F_r$ . Static Equilibrium ..... 77
- Appendix 2.2 Global Safety Factor  $F$  ..... 79
- References..... 80

## Chapter 2

### Catastrophic Slide: Vaiont Landslide, Italy

#### 2.1 *The Landslide*

An impressive double curvature arch dam, 276 m high, was built in the years 1957–1960 to store the waters of the Vaiont River, located in the Italian Alps, approximately 80 km north of the city of Venice. The dam was built in a narrow canyon, cut by the river in massive Jurassic limestone (Fig. 2.1a). The photograph shows, in the foreground, the limestone abutments of the dam and, in the background, the steep slope of the left bank of the river, which was actually the toe of an ancient landslide. The ancient slide became unstable in October 1963, when the level of the reservoir was close to its maximum, and invaded the reservoir at great speed. The displaced water generated a gigantic wave, 220 m high, which flew over the dam (which stood without bursting) and destroyed several villages downstream, causing more than 2,000 casualties. The failure sent seismic waves, recorded in seismographs across Europe.

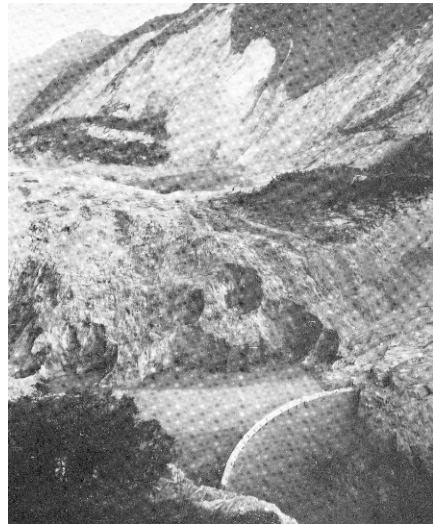
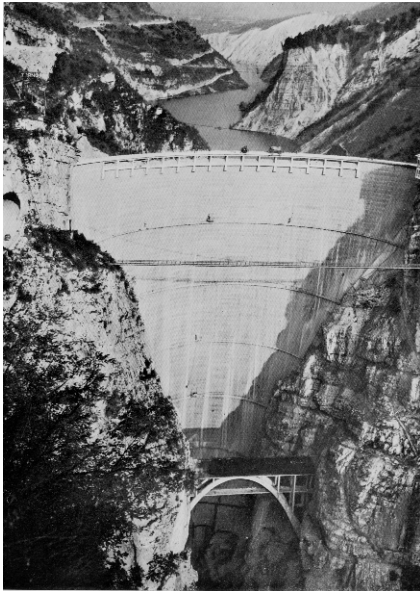


**Figure 2.1** View of Vaiont Dam from downstream: (a) before the catastrophic landslide; (b) after the slide (Valdés Díaz-Caneja, 1964).

Figure 2.1b is a view of the left bank of the river after the slide. The dam, in the lower part of the photograph, was not directly hit by the slide. A small lake

remains between the dam and the toe of the slide. The bridge topping the dam has been destroyed. The slide scarp and a newly created lake may be seen in the background of the photograph. This catastrophe caused a great impact, which was deeply felt by dam and geotechnical engineers around the world.

A brief account of the events leading to the landslide of the left bank of the reservoir is given in the following paragraphs.

Dedicated geological surveys of the left margin of the reservoir started in 1958 under the supervision of L. Müller-Salzburg, an expert in rock mechanics. It was soon realized that a large proportion of the left bank of the reservoir was in fact a very large prehistoric landslide which, sometime in the past, filled the Vaiont valley. The valley had been excavated by the river at the end of the last glacial period (Würm) (Semenza and Ghirotti, 2000). After this prehistoric landslide, the river excavated again a deep valley through the slipped mass. The geological history of the landslide, an aspect which is always of interest in stability problems, is reviewed later.

At the end of 1960, once the dam was built and the reservoir partially impounded, a long, continuous peripheral crack, 1 m wide and 2.5 km in length, marked the contour of a huge mass, creeping towards the reservoir in the northern direction (Fig. 2.2).

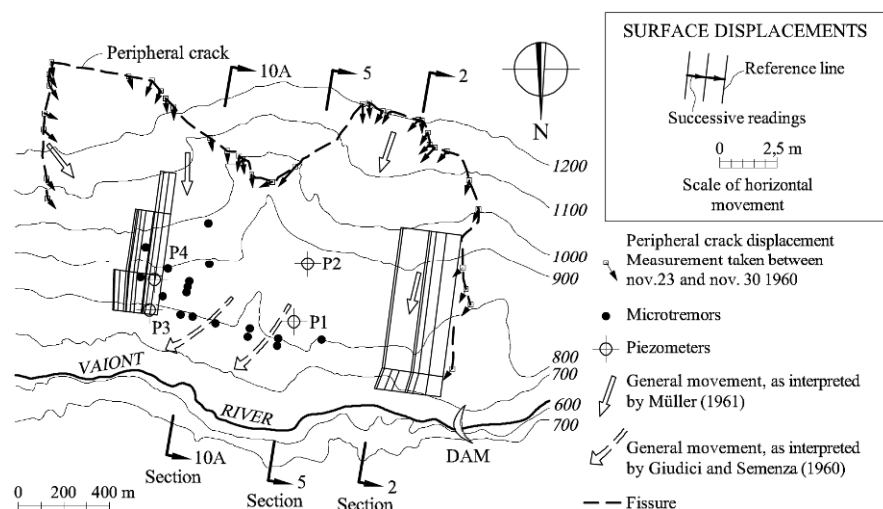


**Figure 2.2** Map of the Vaiont sliding area. Note the position (and comparative size!) of the arch dam on the lower right-hand corner of the figure. (Simplified from Belloni and Stefani (1987) (© 1987 with permission from Elsevier) with additional information from several authors.)

In the following three years, the downward motion of the slide was monitored by means of surface markers. Some of the data provided by them are also plotted in Figure 2.2. In addition, water pressures in perforated pipes, located in four boreholes (location shown in Fig. 2.2), were monitored, starting in July 1961. The

history of rainfall, reservoir level, rate of surface displacement, and water levels in piezometers in the four years preceding the failure is shown in Figure 2.3. Geophysical campaigns were also performed in December 1959 and 1960. Notice also, in Figure 2.3, that two slides of limited size took place during the first partial filling of the reservoir in 1960. Project engineers were by that time convinced that a large landslide could partially fill the reservoir, isolating the dam from the upstream part of the reservoir, and a by-pass tunnel was built in 1961 as a precautionary measure.

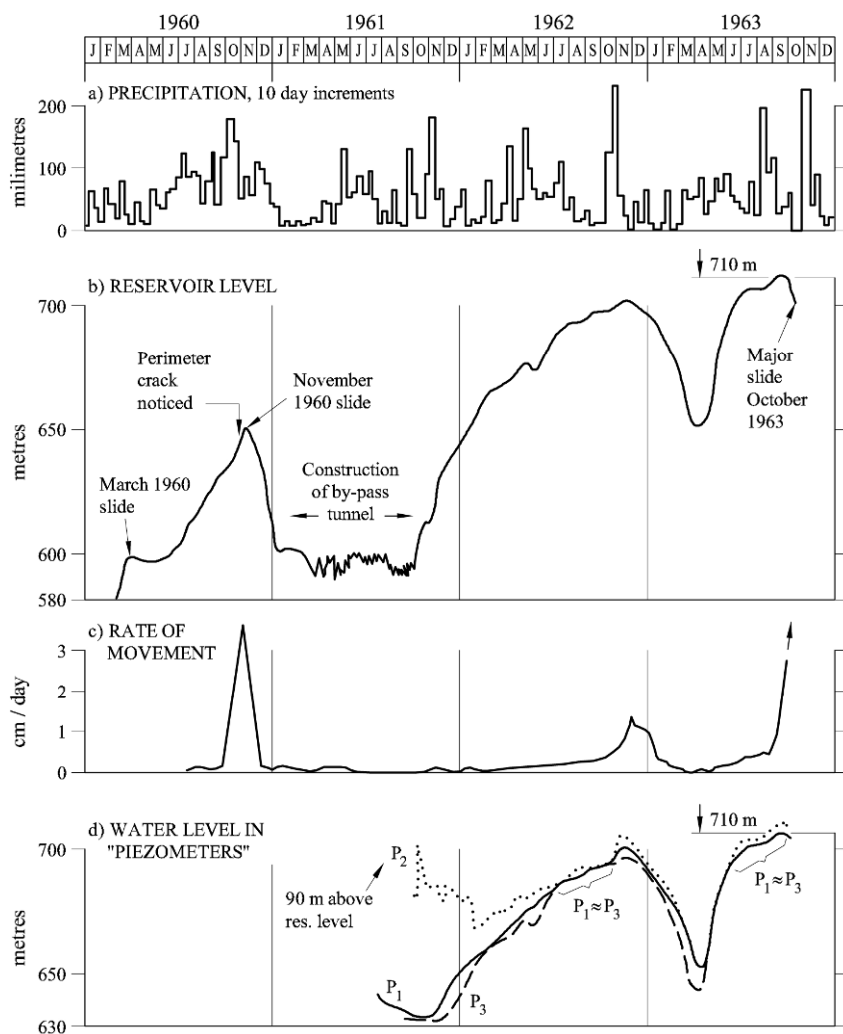


**Figure 2.3** Relationship between precipitation, reservoir elevation, maximum velocity of horizontal surface displacements, and water level in piezometers. (After Hendron and Patton (1985), based on a figure by Müller (1964).)

However, all the investigation efforts provided limited information on some key aspects of the landslide such as the position and shape of the sliding surface and the pore water pressures acting on it. The measured rate of displacements of surface markers could be roughly correlated with the water level of the reservoir (Fig. 2.3). After two cycles of reservoir elevation, which partially filled and emptied the reservoir in the period 1960–1962, the water level reached a maximum (absolute) elevation of 710 m, at the end of September 1963. At that time, the accumulated displacements of surface markers had reached values in excess of 2.50–3 m (Fig. 2.4). The figure shows a good correlation between the increase in water level in the reservoir and the acceleration of the landslide.

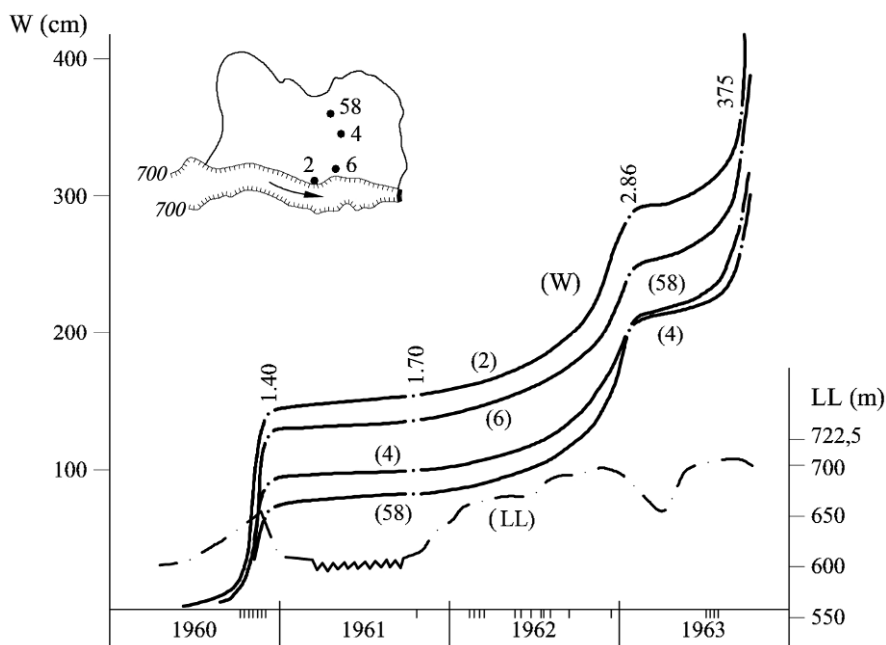


**Figure 2.4** Accumulated displacements of surface markers ( $W$ ) in the period 1960–1963 and its correlation with reservoir elevation ( $LL$ ). Seismic events are marked in the time scale (reprinted from Nonveiller, 1987, © 1987, with permission from Elsevier).

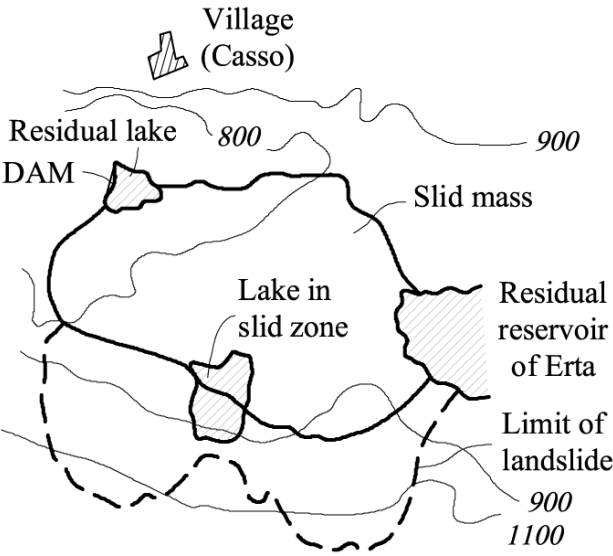
Surface velocities of 20–30 cm per day were registered in the days preceding the final rapid motion that took place in October 9, 1963. An estimated total volume of rock of  $280 \times 10^6 \text{ m}^3$  became unstable, accelerated, and invaded the reservoir at an estimated speed of 30 m/s (around 110 km/hour).

Figure 2.5 is a photograph of the slide taken in 1979. The landslide has filled the valley of the Vaiont River, which can be seen in the background. A residual lake can be seen in the lower left part of the image. The upper planar sliding plane (clear colours) is now exposed. The simplified map in Figure 2.5b, taken from Broili (1967), shows the position of the dam (not seen in the photograph), which

maintains a small reservoir, the residual lake within the sliding area and the contours of the landslide before and after the failure.



(a)



(b)

**Figure 2.5** (a) Photo of the slide area, taken in 1979 (courtesy of G. Fernández); (b) plan view of the area after the slide (Broili, 1967).

The Vaiont landslide has attracted world wide attention concerning the causes and processes involved in the failure. Interest in Vaiont has never decreased within the technical community despite the 47 years that have elapsed since the accident. Papers analyzing the failure have been published at a maintained rate in journals and conferences. The landslide is one of the largest (in terms of volume of mobilized mass) in history. As stated by Hendron and Patton (1987) *“It is likely that more information has been published and more analyses have been made of the Vaiont data than for any other slide in the world”*. This chapter and Chapter 5 are additional contributions to this long list, with the aim of maintaining simplicity, but at the same time with the hope of capturing some fundamental aspects of the failure. Vaiont has been analyzed by researchers in rock and soil mechanics and some specific views of the mechanisms involved in the failure can sometimes be traced to the background of the people conducting the analysis.

One of the main reasons of this interest is the difficulty in explaining the extremely high velocity of the moving mass. The implication of this lack of understanding is that the risk associated with other landslide occurrences of a similar nature (natural slides affected in its toe by increasing water levels, a common situation in dam engineering) cannot be properly evaluated.

The issue of the velocity of the Vaiont landslide will be discussed in Chapter 5. But before this, the conditions for static equilibrium should be understood. Static models, even if they are simple, require an understanding of the main geological, geometrical, hydraulic, and geotechnical features of the slide. In the case of Vaiont, this information should ideally be extended to the old prehistoric landslide, which was reactivated by the reservoir impounding.

## 2.2 Geological Setting

The Vaiont River, which flows from east to west, cuts a large syncline structure which folds Jurassic and Cretaceous strata (Fig. 2.6). The syncline created the “open chair” shape of the Jurassic strata of the left margin of the river, which can also be seen in the figure. The axis of the syncline plunges a few degrees towards the east (normal to the plane of the figure). The syncline shape eventually defined the geometry of the failure surface, which is always important information for understanding the subsequent behaviour of the slide.

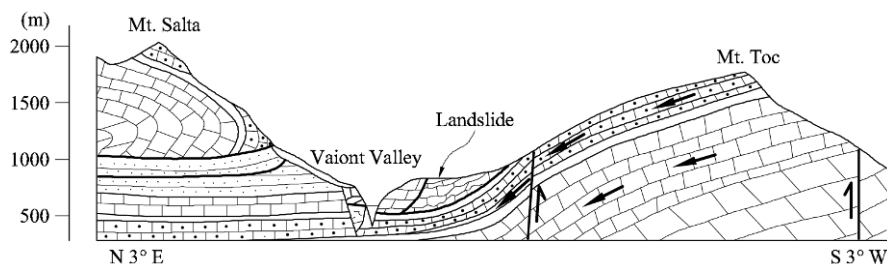


**Figure 2.6** North (Monte Toc) to south (Monte Salta) section showing the general layout of the syncline, the Vaiont gorge and the position of the ancient landslide (after Semenza and Ghirotti, 2000).

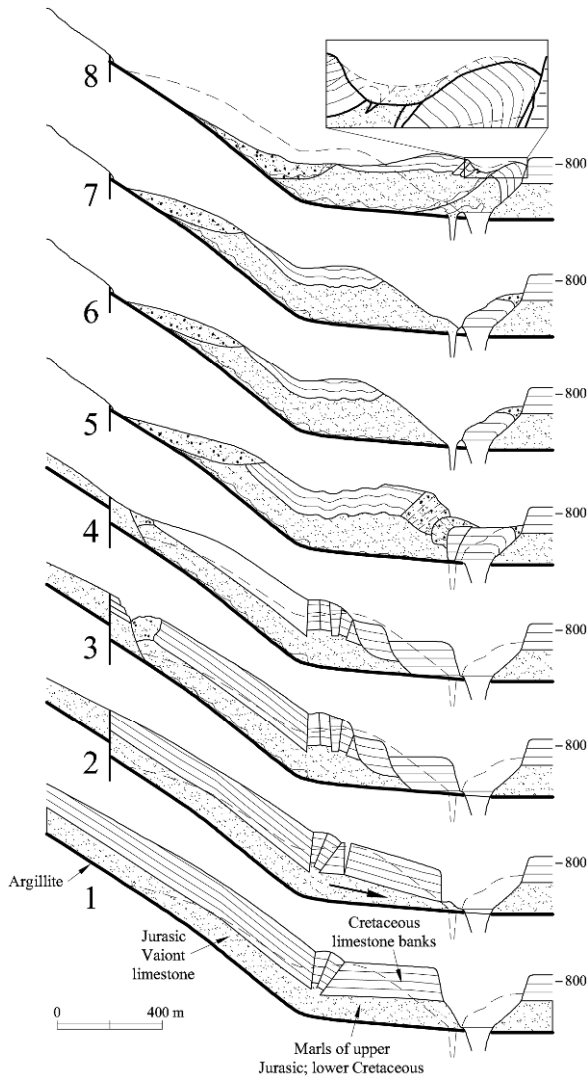


**Figure 2.7** Tentative reconstruction of the paleo-slide of Vaiont. 1: Situation before the first motion (end of last glaciation?); 2: First motion of the slope; 3: Process of progressive sliding (undulated continuous line) and rotational slides at the toe; 4: Successive erosion phenomena on the upper parts; 5: Ancient landslide and intense fracturing of strata. The valley is invaded by the gigantic slide; 6: The slide before November 4, 1960, after thousands of years of erosion. The river has cut a new, narrow gorge; 7: The profile after a “small” landslide on November 4, 1960; 8: The final shape of the cross-section after the slide of October 8, 1963 (present situation). The inset shows an eroded part of the slide surface by the rapidly moving waters displaced by the slide (simplified and adapted from Semenza, 2001).



E. Semenza, an engineering geologist son of the dam designer, made important geological contributions to understand the geology of the site. In his book “La storia del Vaiont raccontata del geologo che ha scoperto la frana” (“The story of Vaiont told by the geologist who discovered the slide”, Semenza, 2001), he includes a tentative reconstruction of the past history of the slide in a series of representative cross-sections, which are reproduced in Figure 2.7.

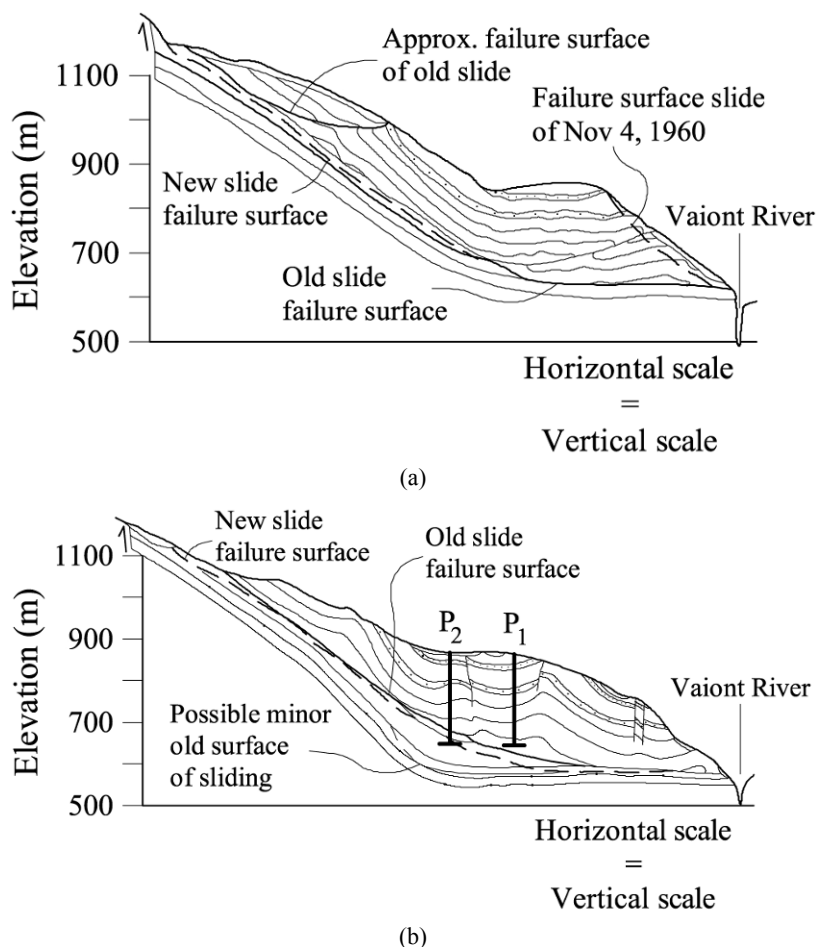


**Figure 2.8** Two representative cross-sections of the landslide: (a) Section 2; (b) Section 5 (see the location in Fig. 2.2). After Hendron and Patton, 1985. The position and length of piezometers  $P_1$  and  $P_2$  are shown on Cross-section 5.

This reconstruction conveys a clear message from a geomechanical point of view: the failure surface, which was probably initiated several tens of thousands of years ago, has been subjected to an ever-increasing story of accumulated relative displacements. The second important point is that the rock mass affected by the

1963 landslide had suffered a history of cracking and “damage” during recent geological times. The sliding surface is located in strata of the upper Malmö period (upper Jurassic). Clays and marls were found in these layers (see the description of the failure surface below). Above the sliding surface, finely stratified layers of marl and limestone from the Malmö period were identified. Below the sliding surface, the Jurassic limestone banks of the Dogger period remained unaffected. In the upper part, limestone strata from the lower Cretaceous crowned the moving mass. In general, the folded layers of limestone and marl were strongly fractured (drilling water was often lost in the exploratory borings performed in 1960).

Two representative cross-sections of the slide, located upstream of the dam’s position at distances of 400 and 600 m, respectively, are reproduced in Figure 2.8 (Sections 2 and 5; Hendron and Patton, 1985). The two cross-sections will be used later to analyze the stability conditions of the landslide.

### 2.3 The Sliding Surface

In their comprehensive report of 1985, Hendron and Patton (1985) describe the detailed investigation performed to identify the nature of the sliding surface. The conclusion is that thin (a few centimetres thick) continuous layers of high plasticity clay were consistently found in the position of the failure surface. A photograph of the surface is shown in Figure 2.9.



**Figure 2.9** A striated continuous clay layer belonging to the sliding surface (courtesy of G. Fernández).

Samples from these clay layers were tested by different laboratories and the results are described in Hendron and Patton (1985). The clays were found to be

Tika and Hutchinson (1999) also examined the effect of the shearing rate. They found (Fig. 2.11b) a further reduction in residual friction which reached low values ( $5^\circ$ ) for shearing rates of 0.1 m/s, a velocity which is still far lower than the estimated sliding velocities of the real failure. However, it is a common experience that increasing strain rate leads to an increase in the strength of soils. More data on the effect of the shearing rate on residual strength is probably needed before reaching definite conclusions on this issue.

Hendron and Patton (1985) estimate that some factors (areas of the sliding surface without clay, some localized shearing across strata, irregularities in the geometry of the sliding surface) could increase the average residual friction angle operating in the field and they estimate that  $\phi'_{\text{res}} = 12^\circ$  is a good approximation for static conditions.

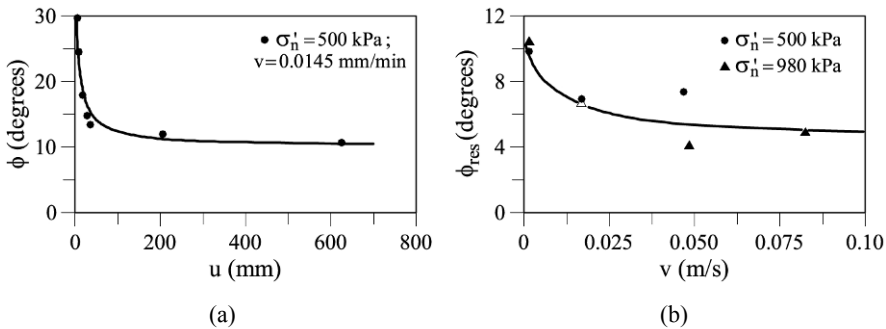


**Figure 2.11** Ring shear tests on a clay specimen from the vicinity of the Vaiont sliding surface: (a) static residual friction determined at a shearing rate of 0.0145 mm/min; (b) effect of shearing rate (Tika and Hutchinson, 1999).

## 2.4 Monitoring Data before the Slide

Significant monitoring data taken during the three years preceding the failure were given in Figures 2.3 and 2.4. The main purpose behind the limited instrumentation available was to relate the level of the reservoir with the measured vertical and horizontal displacements of a number of topographic marks distributed on the slide surface. Data on horizontal displacements, plotted as a function of position and time in several profiles following the south-north direction in Figure 2.2, suggest that the slide was essentially moving as a rigid body. The direction of the slide is also indicated in the figure by several arrows. Some of them (small arrows along the peripheral crack) indicate that the moving mass was actually detaching from the stable rock, implying no friction resistance along the eastern and western boundaries of the slide.

Seismic (volumetric P-wave) velocities were measured in central parts of the slide in December 1959 and again in December 1960. A drop in velocity from  $v_p = 5\text{--}6$  km/s in 1959 to  $v_p = 2.5\text{--}3$  km/s was recorded. This information may be interpreted as an indication of the progressive weakening of the rock mass due to the distortion induced by the creeping motion of the slide. The velocities initially recorded at the end of 1959 are very high and they correspond to a rock of good quality (Barton, 2007). This is perhaps surprising in view of the prehistoric landslide motions described above. The strong drop in seismic velocity in just one year, which is a tiny fraction of time within the complex life of the landslide, seems exaggerated but it is pointing towards significant shear distortions within the rock mass, motivated by the first impoundment of the reservoir which implied a raise of the water level of 200 m (see the history of events in Fig. 2.3). The

associated increase in pore water pressures on the sliding surface is very large and it is unlikely that past rainfall events could have produced such a strong drop in effective stress, especially in the lower part of the slide.

It should be emphasized that these P-wave velocities are much higher than the velocities measured in soils, even if they are dense and compact. In other words, the strength that may be associated with the shearing of the rock mass above the sliding surface is orders of magnitude larger than the strength available at the clay-dominated thin layers at the base of the slide, being sheared along sedimentation planes of very high continuity.

## 2.5 Water Pressures and Rainfall

The position of piezometers (they were open perforated pipes) was indicated, in plan view, in Figure 2.2 and in cross-section in Figure 2.8. A perforated pipe only provides information on the average water pressures crossed by the tube. Note too that the pipes did not reach the position of the sliding surface. Therefore, they did not provide direct information on the water pressures actually existing in the vicinity of the sliding surface, which is fundamental information to perform a drained stability analysis of the landslide.

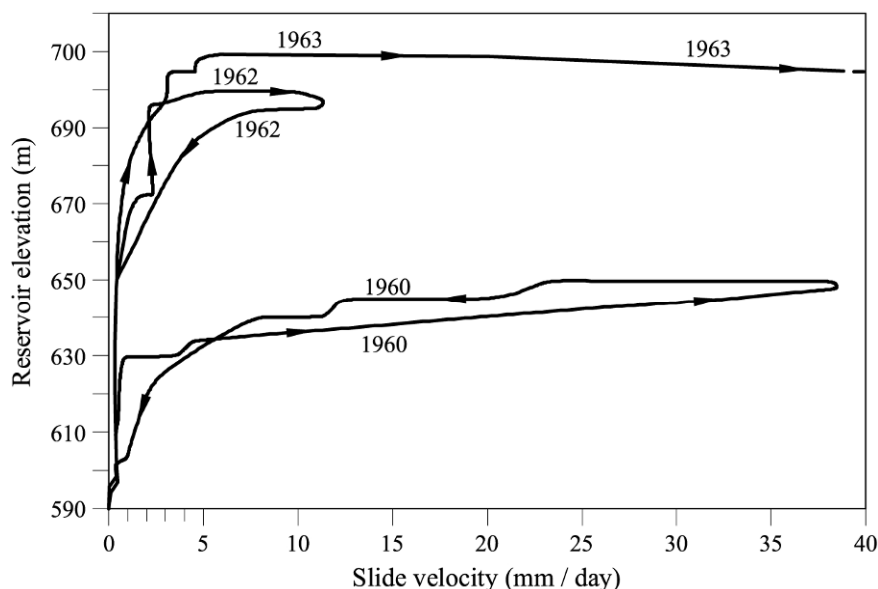


**Figure 2.12** Relationship between water level in the reservoir and sliding velocity (courtesy of G. Fernández).

In general, the water levels recorded by the piezometers follow closely the changing levels of the reservoir (compare Figs. 2.3b and 2.3d). The exception is Piezometer 2, at least during the initial part of the recording period. The initial readings in this piezometer indicated water pressures significantly above (90 m of

water column) the reservoir surface. This information has been interpreted as an indication of additional factors, other than the level in the reservoir, which may control the water pressure at the sliding surface. Since the cretaceous limestone affected by karstic phenomena is a rather pervious mass, rainfall water infiltrating at high elevations may result in artesian pore pressures against the impervious Malmö formations located at the base of the landslide. Arrows showing the circulation of water in Figure 2.6 illustrate this possibility. However, no further and direct evidence of this possibility was recorded. On the other hand, the simultaneous variation of piezometer and reservoir levels is a good indication of the high permeability of the rock mass above the sliding surface.

When the water level in the reservoir is plotted against the recorded slide velocity (Fig. 2.12), an interesting result is obtained. An increasing water level leads to an increase in sliding velocity. The relationship is highly nonlinear and it tends towards an asymptotic limit, which is an indication of failure. The problem with Figure 2.12 is that this relationship is not unique, a result which is not expected if the slide motion is thought to be governed by the effective normal stresses acting on the sliding surface, which, in turn, are controlled by the reservoir level. In fact, the second reservoir filling led to a second asymptotic value for the water level in the reservoir.

This result was probably the main reason behind the decision to increase the water level for the third time in search of a higher (but safe) level in the reservoir, which would allow the normal operation of the dam. The idea behind this decision, apparently put forward by L. Müller, is that the rock reacts in a different way when it is wetted for the first time, compared with its reaction when it has previously been wetted. There is no fundamental mechanical basis for this proposition, however. The fact is that, during the third attempt to raise the water level, displacement velocities increased continuously and the final attempts to reduce the velocity of the slide, by lowering the level of the reservoir (Fig. 2.3b), did not work.

An explanation for the apparent inconsistency of results in Figure 2.12 could be found if the reservoir water level and rainfall are combined in the spirit that the prevailing water pressures on the sliding surface, irrespective of their origin, should control the stability.

Hendron and Patton (1985) found a reasonably good explanation if rainfall, averaged over the preceding 30 days, and water level are jointly considered to explain the landslide velocity (Fig. 2.13). The boundary line between “stable” and “unstable” situations, plotted in Figure 2.13, could even provide the equivalent reservoir elevation for a given rainfall intensity.

The actual failure occurred for a 30-day precipitation of 240 mm, when the reservoir was at an elevation of 700 m. Leonards (1987) analyzed further the rainfall records and the history of reservoir elevation and could not find a satisfactory explanation, free of inconsistencies, for the relationship between velocities of the slide, reservoir elevation, and previous rainfall. The pore pressure regime prevailing at the sliding surface remains rather uncertain in the Vaiont landslide.

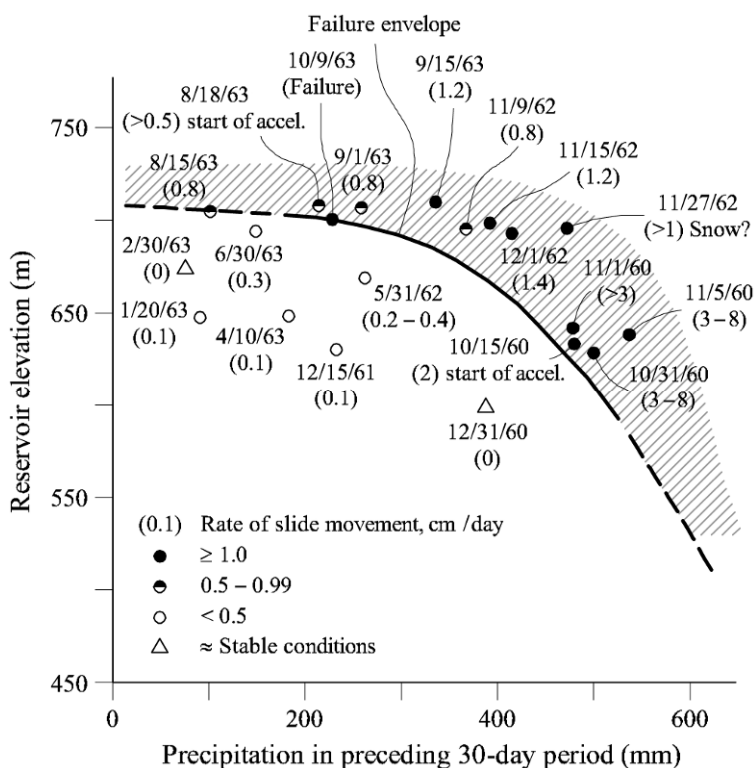


**Figure 2.13** Sliding rate related with precipitation (averaged over the preceding 30-day period) and reservoir elevation (Hendron and Patton, 1985).

## 2.6 A Simple Stability Model

The two representative cross-sections, 2 and 5 in Figure 2.8, are represented in Figure 2.14 in a simplified version, which is, however, close to the original drawings. The two plots highlight that the failure surface could be described by two planes: a lower horizontal plane daylighting at the river canyon wall and an inclined planar surface. A rock wedge whose thickness decreases upwards rests on the inclined plane. The rock mass reaches its maximum thickness, 270 m, in the central lower part of the slide, above the horizontal sliding plane.

A good proportion of reported stability analyses of Vaiont, especially in the years following the failure, have concentrated on the determination of the friction angle necessary for stability (Jaeger, 1965; Nonveiller, 1967; Mencl, 1966; Skempton, 1966; Kenney, 1967). Classic procedures for stability analysis in soil mechanics using limit equilibrium methods were used. These methods explain the instability for friction angles in the range  $18 - 28^\circ$ . The preceding account of the relevant information on Vaiont, namely the data presented by Hendron and Patton (1985) indicates, however, that the friction angle at the failure surface could hardly be larger than 12 degrees.

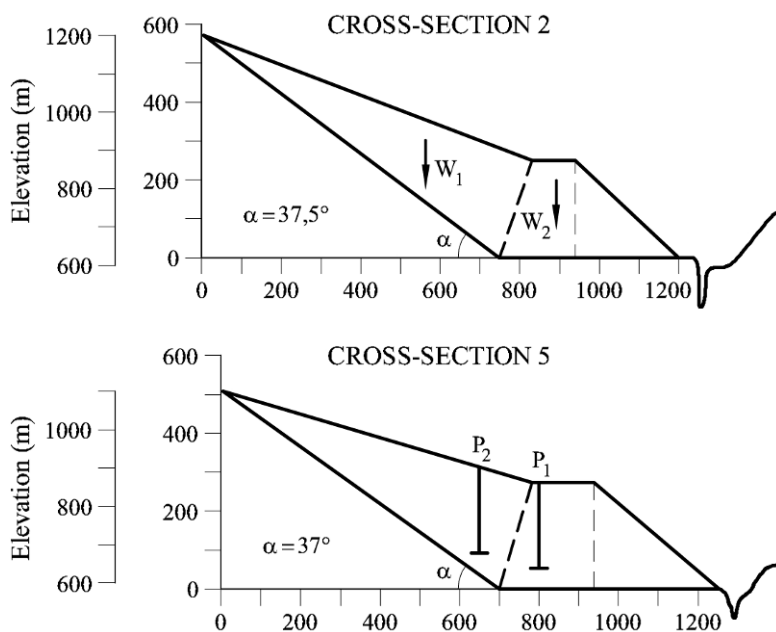


**Figure 2.14** Cross-sections 2 and 5 of the Vaiont landslide. Initial geometry.

Two main reasons support this statement: the fact that Vaiont was a case of landslide reactivation (which implies large previous shearing displacements at the sliding surface and, hence, a clear situation of residual strength conditions) and the small residual friction angles (8–10°) measured in the highly plastic clays (Ca-montmorillonite rich) associated with the sliding surface. Therefore, a relevant question is: are the representative cross-sections in Figure 2.14 stable, given the value of the basal friction angle and the estimated conditions of pore water pressure, when the reservoir reached elevations in the range of 650 to 700 m?

The cross-sections plotted in Figure 2.14 suggest that the slide may be defined as two interacting wedges: an upper one (Wedge 1) sliding on a plane having a dip of 36–37° and a lower one (Wedge 2) sliding on a horizontal plane. Since a (common) friction angle of 12 degrees is acting at the basal sliding surfaces, the upper wedge is intrinsically unstable and will push the lower resisting wedge. The weights of the two wedges and the distribution of pore water pressures prevailing on the sliding plane will, as a first approximation, dictate the stability conditions. However, the interaction between the two wedges also plays a relevant role in explaining the stability, as discussed below.

### 2.6.1 Kinematics of the slide

It is worth at this point to examine the kinematics of the slide. If the motion starts, one may imagine the slide as a train sliding downwards, an image which is brought to justify that the absolute velocity in the upper and lower parts of the



slide are essentially the same. Surveying data plotted in Figure 2.2 support this simple hypothesis, which is to be expected in the reactivation of an old landslide. The difference in velocity (or displacement) when comparing the upper and lower parts of the slide obviously lies in the direction of these vectors: they will be parallel to the underlying failure surface. A conflict arises, however, at the kink or junction between the two sliding planes. Within the train analogy, if the wagon passing over this kink is to maintain contact with the kinked rail, it will be bent and sheared. It is hard to imagine that voids will develop in the layered sequence of marl and limestone at 270 m depth. The alternative is the bending and shearing of strata. In fact, a single shearing plane may be invoked to accommodate the sudden change in the direction of velocity at the kink. This is indicated in Figure 2.15, where sliding velocity vectors  $\mathbf{v}_1$  (in the direction of the upper inclined surface) and  $\mathbf{v}_2$  (horizontal, parallel to the basal plane) are plotted with a common origin. This velocity diagram represents the conditions at the kink (point A), where the rock approaches A with velocity  $\mathbf{v}_1$  and leaves it with velocity  $\mathbf{v}_2$ . Since the absolute velocity of the two wedges is the same, the relative motion of the two wedges (vector  $\mathbf{v}_{12}$ ) is directed in the direction of the bisector of the angle between the upper and lower sliding surfaces. Therefore, a change in the direction of the velocities of the two wedges may be accommodated by a relative shear in the direction of the bisector plane, plotted in Figure 2.14.

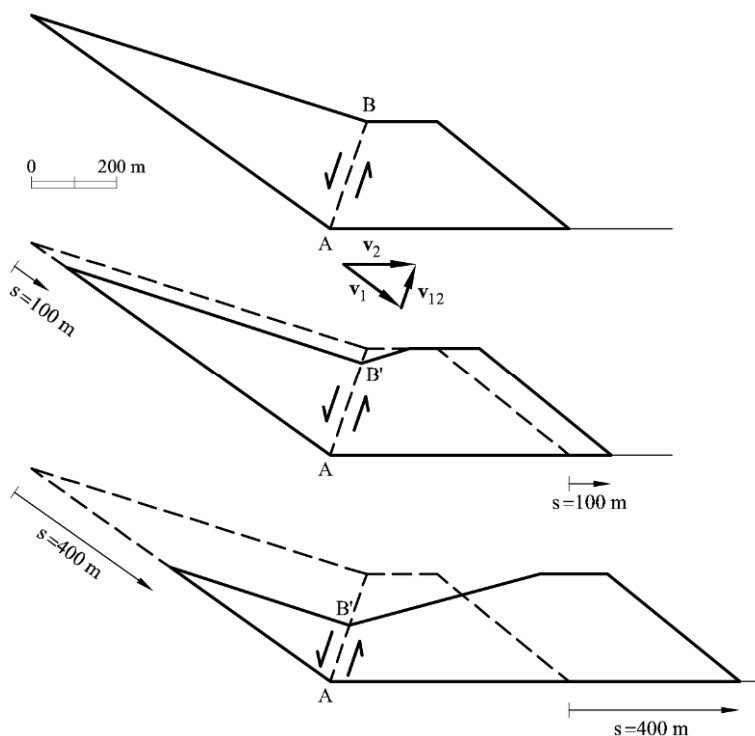


**Figure 2.15** Kinematics of sliding. Section 5.

The motion of the slide implies that the (unstable) mass from the upper wedge becomes the (stable) mass of the lower wedge. In this process, the sliding resistance along the common plane separating the two wedges has to be overcome. If it is accepted, because of the preceding discussion, that the common plane of intense shear bounding the two wedges is the bisector plane (Fig. 2.15), the evolution of the geometry of the sliding mass may be approximated by the successive cross-sections shown in Figure 2.15 for total slide displacements  $s = 0$  m,  $s = 100$  m and  $s = 400$  m. Figure 2.15 is a graphic expression of the condition of mass conservation during landslide motion. It will be used later to perform a dynamic analysis of the failure.

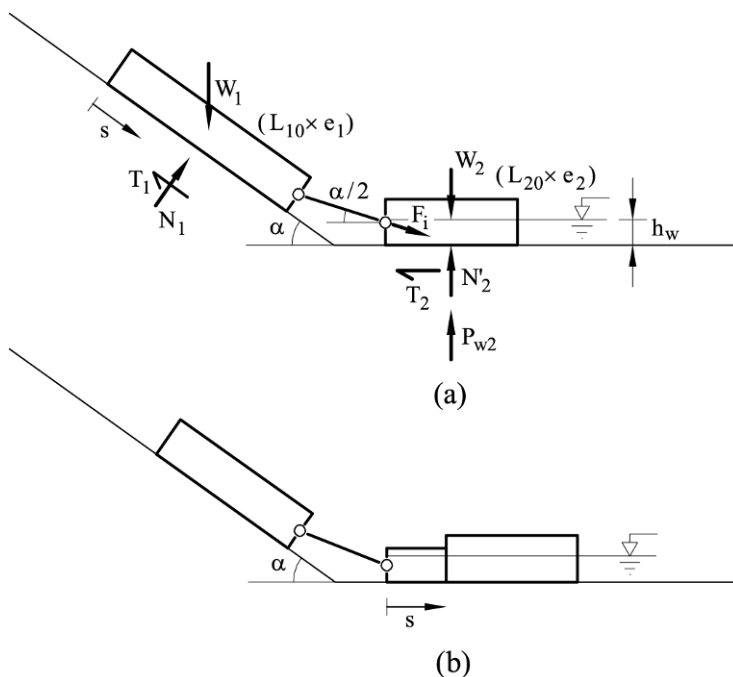


**Figure 2.16** Two-block model of the Vaiont slide: (a) definition of geometry and forces (initial stage); (b) the slide after a displacement  $s$ .

### 2.6.2 Two-block model

Consider in Figure 2.16, the “unstable” and “stable” blocks mentioned before in a very simple representation: two solid blocks connected by double hinged bar normal to the bisector plane. The interaction between the two blocks is simply given by a force,  $F_i$ . Note that this force introduces normal and shear forces on the common plane between the two blocks. The lower block is partially submerged and the level of water has a height  $h_w$  with respect to the lower horizontal sliding plane. The upper block is not affected by water.

The sketch in Figure 2.16a provides a definition of forces acting on each

block. A simple problem is defined as follows: find the angle of basal shearing resistance for equilibrium. This is an elementary problem in mechanics which is solved by expressing equilibrium of forces for each block and then forcing a common value for the interaction between the two blocks. Static equilibrium expressions (normal and parallel to the direction of sliding) are written as follows, in terms of effective stresses:

- Upper block 1:

$$W_1 \cos \alpha + F_i \sin(\alpha / 2) = N_1, \quad (2.1a)$$

$$W_1 \sin \alpha = T_1 + F_i \cos(\alpha / 2), \quad (2.1b)$$

$$T_1 = N_1 \tan \phi'_b, \quad (2.1c)$$

since no water is acting on the upper sliding block,  $N_1 = N'_1$ .

- Lower block 2:

$$W_2 + F_i \sin(\alpha / 2) = N'_2 + P_{w2}, \quad (2.2a)$$

$$F_i \cos(\alpha / 2) = T_2, \quad (2.2b)$$

$$T_2 = N'_2 \tan \phi'_b, \quad (2.2c)$$

where  $\tan \phi'_b$  is the effective friction coefficient on the sliding planes.

Isolating  $F_i$  in (2.1) and (2.2), respectively, and making them equal, results in

$$\frac{W_1 (\sin \alpha - \cos \alpha \tan \phi'_b)}{\sin(\alpha / 2) \tan \phi'_b + \cos(\alpha / 2)} = \frac{(W_2 - P_{w2}) \tan \phi'_b}{\cos(\alpha / 2) - \tan \phi'_b \sin(\alpha / 2)}, \quad (2.3)$$

which is a second-order algebraic equation for  $\tan \phi'_b$ . The volumes of blocks 1 and 2 are estimated as follows for Section 5:  $V_{10} = 112,590 \text{ m}^3/\text{m}$  and  $V_{20} = 93,000 \text{ m}^3/\text{m}$ , where the subscript <sub>0</sub> indicates initial value (no displacement of the slide). The indicated volumes correspond to a landslide “slice”, one meter thick.

The value of  $P_{w2}$  may be calculated as  $P_{w2} = L_{20} h_w$  if a length for Block 2 is estimated. The length of the basal horizontal plane in Figures 2.14 or 2.15 is  $L_{20} = 560 \text{ m}$ . Finally, a specific weight,  $\gamma_r = 23.5 \text{ kN/m}^3$  was taken for the rock in order to compute the weights of the blocks. Accepting these values, the following friction angles are derived for Cross-section 5 ( $\alpha = 37^\circ$ ):

$$\phi'_b = 21.1^\circ \text{ for } h_w = 120 \text{ m},$$

$$\phi'_b = 19.4^\circ \text{ for } h_w = 60 \text{ m}.$$

The lower horizontal plane in Section 5 is approximately at elevation 590 m (Fig. 2.13) and the maximum reservoir level attained was 710 m (Fig. 2.3).

Therefore, the first case defines the maximum water pressure experienced by the lower block before the failure. Slide displacements (which, in practice, are interpreted as a condition of strict static equilibrium) were also recorded at lower water elevations ( $h_w = 60$  m, which corresponds to the situation in November 1960, see Fig. 2.3). However, the actual pore water pressure is also controlled by the rainfall regime, as previously discussed, and uncertainties remain on the actual value of the operating pore water pressures against the sliding surface.

Despite its simplicity, the block model provides some hints on the effect of water level and slide displacement on safety factor. If  $\phi'_b = 21.1^\circ$  is taken as the real effective friction angle along the failure surface, the safety factor,  $F$ , is defined as

$$F = \frac{\tan(21.1^\circ)}{\tan(\phi'_{\text{mob}})},$$

where  $\phi'_{\text{mob}}$  is the “mobilized” friction angle, i.e. the friction angle that ensures strict equilibrium for another situation of the slide and, in particular, for changing water levels in the reservoir. Values of  $\phi'_{\text{mob}}$  were calculated through Equation (2.3) for different values of  $h_w$  and the calculated safety factor is plotted in Figure 2.17a. The explanation of this figure is straightforward: as water level increases, it reduces the effective weight of the lower block,  $(W_2 - P_{w2})$ , and the friction required for equilibrium has to increase. Note, however, that the upper block is not affected by the water level in this simplified model, a situation that may change in other cases. In Vaiont, as shown later, the maximum reservoir level introduces pore water pressures in the lower part of the upper wedge. It should be added that the trend shown in Figure 2.17a (decreasing safety factor as the water level increases) is not a general result for other slide geometries and stronger changes in water elevation.

The effect of changing geometry as the slide is set in motion, may be also analyzed. Figure 2.16b includes a proposal to transfer mass from the upper block to the lower one. It is a rough approximation to the more refined model sketched in Figure 2.15. It simply states that the current weights of the two blocks, for a slide displacement  $s$  is given by

$$W_1 = W_{10} - e_1 s \gamma_r, \quad (2.4a)$$

$$W_2 = W_{20} + e_1 s \gamma_r, \quad (2.4b)$$

where  $e_1$  is the thickness of the upper block ( $V_{10} = L_{10}e_1$ ; for Section 5,  $L_{10} = 700$  m and the volume of the upper block is  $V_{10} = 112,590 \text{ m}^3/\text{m}$ ; therefore,  $e_1 = 160.8$  m). In addition, the water uplift under block 2 is calculated as  $P_{w2} = (L_{20} + s)h_w$ .

Equation (2.3) provides again the value of  $\phi'_{\text{mob}}$  for the current weights, and therefore safety factors may be found for increasing slide displacements. They are plotted in Figure 2.17b, for Cross-section 5. The result is to be expected: the moving slide becomes progressively more stable because the lower stabilizing

weight increases at the expense of the upper unstable block whose mass is continuously decreasing.

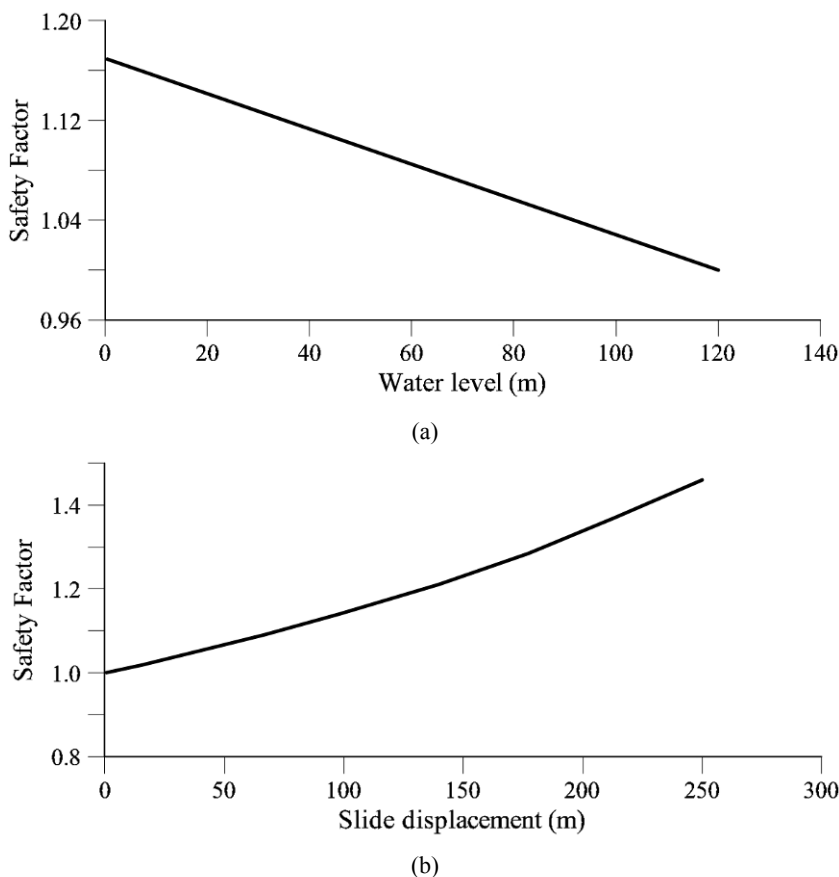


**Figure 2.17** Two-block model. Effect of (a) water level – for zero displacement – and (b) slide displacement – for  $h_w = 120$  m – on safety factor. Section 5.

Unfortunately, the real behaviour of Vaiont was totally different: it accelerated downwards despite the prediction of the simple two-block model. Somehow, the resisting forces had to decrease substantially in order to transform a self-stabilizing mechanism (the two-block model) into an increasingly unstable mass, able to accelerate.

The two-block model has a further limitation: the effective friction angle for equilibrium ( $\phi'_b = 21.1^\circ$  for  $h_w = 120$  m or  $\phi'_b = 19.4^\circ$  for  $h_w = 60$  m, both in Cross-section 5; the “small” difference is non-relevant here) is far higher than the residual friction angle,  $\phi'_{res} = 12^\circ$ , which is the most likely value as justified above. This is an inconsistent result which indicates that the simple two-block

model is too crude to represent the actual conditions of the Vaiont slide (equally inconsistent results are obtained for Cross-section 2).

The next step will be to remove some of the limitations of the simple two-block model in order to approximate more realistically the sliding conditions summarized in Figure 2.15.

### 2.6.3 Two interacting wedges

Shearing across the common plane AB between the upper and lower wedges (Fig. 2.15) has a direction approximately perpendicular to the sedimentation planes of marls and limestones of the Malmö period overlying the failure surface. The shear resistance offered by plane AB is difficult to estimate because of the intricate geometry involved at several scales and the limited continuity of joints. Some researchers in rock mechanics, notably E. Hoek, have made efforts to provide an answer to this difficult problem from a practical perspective. An account of Hoek's work may be found in the rock mechanics textbook (Hoek, 2007).

Following Hoek, the strength of rock masses may be approximated if some basic characteristics are determined (rock matrix unconfined strength; degree of jointing and state of the surfaces, lithology, etc.). As an example, Figure 2.18 shows the strength envelope in a Mohr stress plane for a rock mass that may approximate the Malmö layers above the sliding surface of Vaiont. The envelope was defined using the free access "virtual laboratory" found on the preceding web page. Details of the defined rock mass are given in the caption of Figure 2.18. It may correspond to the Vaiont rock mass, which was described as follows by Müller (1987), after the failure:

*"The part of the stratigraphic column exposed in the slide mass consists of beds of partially crystalline limestones, limestones with hard siliceous inclusions, marly limestones, and marls. Many beds are strongly folded and show indications of slope tectonics. Its geological structure and also its geological sequence has remained essentially unchanged. The entire rock mass remained intact and the sediment facies is nearly unchanged. Apart from some newly formed faults, the only other effects of the slide were the opening of existing joints and the development of new joints, resulting in an overall volume increase of 4 – 6% and an associated reduction of the mechanical coherence of the rock mass."*

The strength envelope is nonlinear but a Mohr–Coulomb approximation is also shown in Figure 2.18 for a range of normal stresses centered at  $\sigma'_n = 2$  MPa, a stress which may represent average conditions on the bisector plane AB (Fig. 2.15). The Mohr–Coulomb strength parameters ( $c'_r = 0.787$  MPa;  $\phi'_r = 38.5^\circ$ ) define the linear Mohr–Coulomb approximation in Figure 2.18.

The relevant point is that the shear plane AB may offer a substantial resistance to be sheared and this resistance probably has a significant role in stability. Shearing across a rock mass is typically associated with the release of energy. In fact, in the years preceding the failure, when three attempts to fill the reservoir were made, seismic events were recorded on the slide surface. Their location is plotted in Figure 2.2. They approximately span, in plan view, the position of the shear plane AB plotted in Figure 2.15. Nonveiller (1987), quoting a report on

these shocks mentions that “[...] the shocks generated in the zone of the slide signify dilation of the material in a zone of sagging of the rock”.

These events had an increasing frequency in periods of slide acceleration, when the reservoir level increased. This is shown in Figure 2.4, where seismic events are plotted as small marks on the time axis (lower part of the figure).

It was also reported that the rock experienced a global degradation, reflected in a substantial drop of P-wave velocities, as a result of the slide motion during the period December 1959–December 1960. All this evidence supports the conclusion that a rock mass around the position of the ideal shear plane AB was subjected to intense shearing during the cycles of filling and emptying the reservoir in the years previous to the failure.

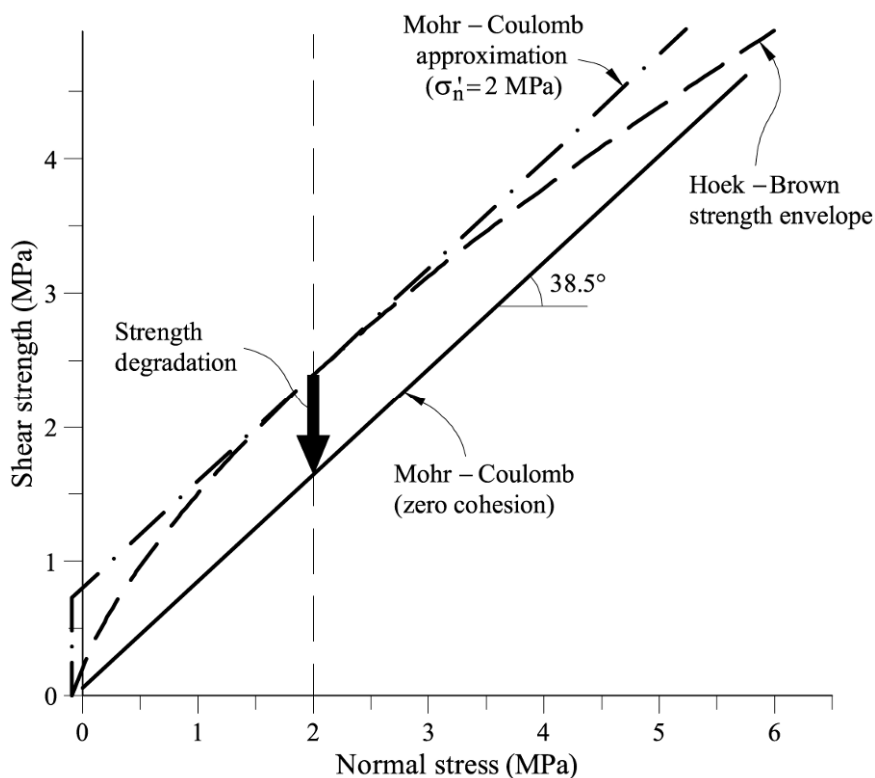


**Figure 2.18** Strength envelope of a rock mass described as: strength of intact material: 50 MPa (limestone-claystone); Hoek Geological Strength Index (GSI = 50) (very blocky, interlocked, and partially disturbed, with multifaceted angular blocks formed by four or more joint sets), Hoek  $m_i$  parameter  $m_i = 9$  (marls, soft limestones); degradation parameter  $D = 0.5$  (in a scale 0 to 1) (according to the Hoek – Brown classification of rock masses; see [www.rocscience.com](http://www.rocscience.com)). Also shown is the Mohr – Coulomb approximation for a normal stress of 2 MPa ( $c'_r = 0.787$  MPa,  $\phi'_r = 38.5^\circ$ ) and an arrow showing the degradation of cohesive intercept at constant  $\phi'_r$  value.

A loss of strength (*reduction of mechanical coherence* in Müller's words) was certainly a consequence of this straining. Typically, cohesion is first lost but friction tends to remain without much change. This drop of cohesion as a result of straining along plane AB was shown in Figure 2.18. In the model described below, the apparent cohesion in the shear plane AB will be reduced as the slide moves forward.

Going back again to Figure 2.15, as slide displacement increases, "new" planes of rock cross the shearing position AB that remains fixed at the position of the bisector plane, which is independent of the slide motion. The consequence is that the shear strength along this plane will not decrease in a sudden and intense manner. Certainly, the motion of the slide will have some weakening effect, which is difficult to quantify. Finally, to complicate matters, progressive failure mechanisms along AB are to be expected in view of the brittle nature of rock strength, a phenomenon which will not be considered here but is mentioned because it will tend to partially destroy the strength available along shear plane AB.

A model based on the interaction of two wedges will now be developed. The main assumptions are:

- The upper and lower wedges change their geometry during sliding, as shown in Figure 2.15. The upper wedge loses mass which is added to the lower one.
- During the movement, the common plane AB reduces in length. Shearing across this plane (or, more generally, AB') is described by a Mohr-Coulomb strength criterion ( $\tau = c'_r + \sigma' \tan \phi'_r$ ). In addition, the cohesive intercept,  $c'_r$ , is made dependent on slide displacement,  $s$ . This is a simplified procedure to introduce strength degradation of the rock mass during the slide motion. The friction angle is maintained constant.
- The lower sliding surface is assumed to be in residual conditions with strength parameters ( $c' = 0$ ;  $\phi'_b = 12^\circ$ ).
- Pore water pressures are given by a horizontal phreatic level.
- Equilibrium conditions are formulated in dynamic terms. In this way, it will be possible to analyze the effect of strength degradation of shearing plane AB' on slide motion. Static conditions of equilibrium are a particular case of the dynamic case. Only inertia terms are considered. No viscous effects are introduced.

The analysis follows the general procedure advanced before when considering the two hinged blocks but now dynamic equilibrium is formulated: Newton's Second Law will be written for the upper and lower wedge, and a common interaction force across plane AB will be enforced. Newton's second law for a solid body motion states that the derivative of the solid momentum (mass times velocity) is balanced by the sum of forces acting on the body. Note that the mass of each wedge depends on displacement and therefore the term of time variation of mass can not be simplified when the time derivative of momentum is developed.



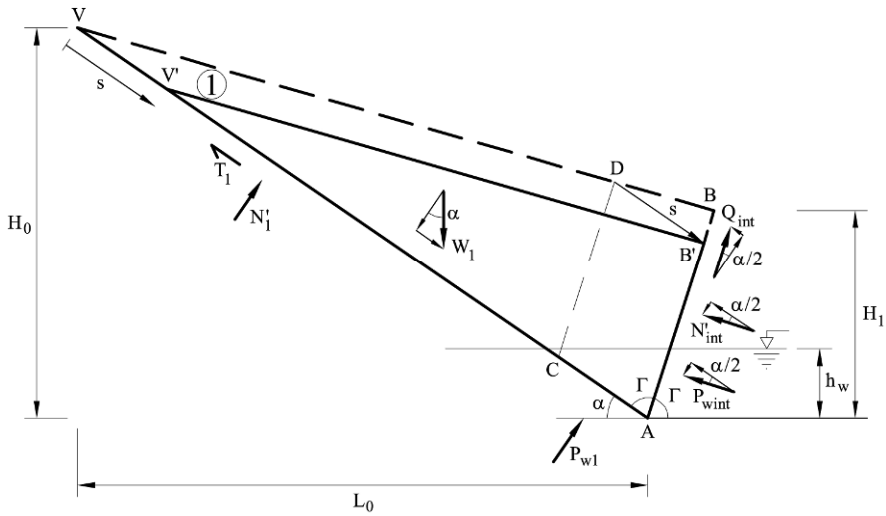


**Figure 2.19** Geometry and forces on the upper wedge (1).

### Upper Wedge (1)

Consider the wedge geometry and external forces in Figure 2.19. Dynamic equilibrium parallel to the motion (displacement  $s$ ; velocity  $v = ds/dt$ ) reads

$$W_1 \sin \alpha - T_1 - N'_{\text{int}} \cos(\alpha/2) - Q_{\text{int}} \sin(\alpha/2) - P_{\text{wint}} \cos(\alpha/2) = \frac{d(M_1 v)}{dt}, \quad (2.5)$$

where  $M_1$  is the mass of Wedge 1, ( $W_1 = M_1 g$ ;  $g$ : gravity acceleration). The time derivative of the right-hand side of Equation (2.5) can be developed as

$$\frac{d(M_1 v)}{dt} = M_1 \frac{dv}{dt} + \frac{dM_1}{dt} v \quad (2.6)$$

Equilibrium in normal direction to the basal sliding plane:

$$W_1 \cos \alpha - N'_1 + N'_{\text{int}} \sin(\alpha/2) - Q_{\text{int}} \cos(\alpha/2) - P_{\text{w1}} + P_{\text{wint}} \sin(\alpha/2) = 0 \quad (2.7)$$

where the interaction forces  $Q_{\text{int}}$  and  $N'_{\text{int}}$  are related through

$$Q_{\text{int}} = c'_r AB' + N'_{\text{int}} \tan \phi'_r. \quad (2.8)$$

In addition, the shear resistance on the base of the wedge is given by

$$T_1 = N'_1 \tan \phi'_b. \quad (2.9)$$

The motion Equation (2.5), in view of (2.7), (2.8), and (2.9), becomes

$$W_1 s_1 - N'_{\text{int}} s_2 + c'_r AB' s_3 - P_{\text{wint}} s_4 + P_{\text{w1}} \tan \phi'_b = \frac{d(M_1 v)}{dt}, \quad (2.10)$$

where  $s_i$  are trigonometric constants, given by

$$s_1 = \sin \alpha - \tan \phi'_b \cos \alpha, \quad (2.11a)$$

$$s_2 = \tan \phi'_b \sin(\alpha/2) - \cos(\alpha/2) \tan \phi'_r \tan \phi'_b + \cos(\alpha/2) + \sin(\alpha/2) \tan \phi'_r, \quad (2.11b)$$

$$s_3 = \tan \phi'_b \cos(\alpha/2) - \sin(\alpha/2), \quad (2.11c)$$

$$s_4 = \tan \phi'_b \sin(\alpha/2) + \cos(\alpha/2). \quad (2.11d)$$

The effective interaction normal force, at this stage unknown, can be isolated from Equation (2.10):

$$N'_{\text{int}} = \frac{1}{s_2} \left( W_1 s_1 + c'_r AB' s_3 - P_{\text{wint}} s_4 + P_{\text{wl}} \tan \phi'_b - \frac{d(M_1 v)}{dt} \right). \quad (2.12)$$

When the wedge slides a distance  $s$  along the basal plane, the length of the shear plane reduces from  $AB$  to  $AB'$  (Fig. 2.19). Since triangles  $AVB$  and  $AV'B'$  are similar, it is easy to find

$$AB' = \frac{L_0 / \cos \alpha - s}{L_0 / \cos \alpha} \frac{H_1}{\cos(\alpha/2)}, \quad (2.13)$$

where  $H_1$  is the initial thickness of the lower wedge over the sliding plane (Fig. 2.19).

The volume of Wedge 1 can be expressed as a function of the initial geometric parameters and the displacement  $s$  as

$$V_{\text{Wedge 1}} = \frac{1}{2} \left( \frac{L_0}{\cos \alpha} - s \right)^2 \frac{H_1}{L_0} \frac{\cos \alpha}{\cos(\alpha/2)} \quad (2.14)$$

The mass and weight of the wedge can be now easily calculated by multiplying the volume of Equation 2.14 by the density ( $\delta_r$ ) and unit weight ( $\gamma_r$ ) of the rock, respectively.

Time variation of mass can be obtained as follow:

$$\frac{dM_1}{dt} = \delta_r \frac{dV_{\text{Wedge 1}}}{dt} = -\delta_r \left( \frac{L_0}{\cos \alpha} - s \right) \frac{H_1}{L_0} \frac{\cos \alpha}{\cos(\alpha/2)} \frac{ds}{dt}, \quad (2.15)$$

where the time variation of the displacement ( $\frac{ds}{dt}$ ) is equal to the velocity  $v$ .

#### Lower wedge (2)

The wedge geometry and external forces are given in Figure 2.20. The wedge is

shown displaced forward at distance  $s$ .

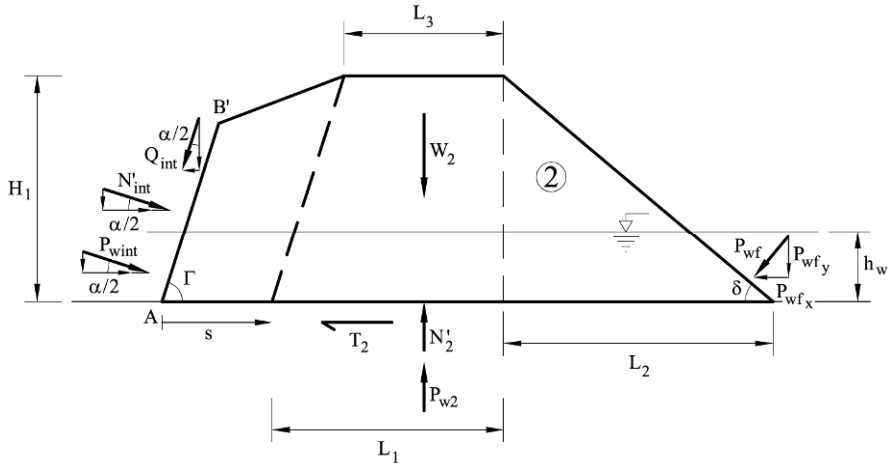


**Figure 2.20** Geometry and forces on the lower wedge (2).

Dynamic equilibrium parallel to the direction of motion at a velocity  $v = ds/dt$  reads

$$N'_{\text{int}} \cos(\alpha/2) - Q_{\text{int}} \sin(\alpha/2) - T_2 = \frac{d(M_2 v)}{dt}, \quad (2.16)$$

where  $M_2$  is the mass of Wedge 2 ( $W_2 = M_2 g$ ;  $g$ : gravity acceleration). Note that the horizontal components of the water pressure forces  $P_{w\text{int}}$  and  $P_{wf}$  acting on the slope surface are equal and opposite in sign. The terms on the right-hand side of the Equation (2.16) can be developed following Equation (2.6) and, since the total mass of the slide is constant, the time variation of  $M_2$  will be equal to the time variation of  $M_1$  indicated in Equation (2.6) but with an opposite sign.

The base resistance is given by

$$T_2 = N'_2 \tan \phi'_b. \quad (2.17)$$

Taking Equation (2.8) into account, Equation (2.16) becomes

$$N'_{\text{int}} \cos(\alpha/2) - N'_2 \tan \phi'_b - (c'_r AB' + N'_{\text{int}} \tan \phi'_r) \sin(\alpha/2) = \frac{d(M_2 v)}{dt}. \quad (2.18)$$

Equilibrium in a normal direction to the horizontal sliding plane reads:

$$W_2 - N'_2 + N'_{\text{int}} \sin(\alpha/2) + (c'_r AB' + N'_{\text{int}} \tan \phi'_r) \cos(\alpha/2) + P_{w\text{int}} \sin(\alpha/2) + P_{wf_y} - P_{w2} = 0. \quad (2.19)$$

Equation (2.19) provides an expression for  $N'_2$  which is introduced in Equation (2.18). The following expression is then found for the equation of motion in the

direction of sliding:

$$N'_{\text{int}} s_5 - c'_r AB' s_6 - P_{\text{wint}} s_7 + (P_{w2} - P_{wfy} - W_2) \tan \phi'_b = \frac{d(M_2 v)}{dt}, \quad (2.20)$$

where  $s_i$  are trigonometric constants given by

$$s_5 = \cos(\alpha/2) - \tan \phi'_b \sin(\alpha/2) - \cos(\alpha/2) \tan \phi'_r \tan \phi'_b - \sin(\alpha/2) \tan \phi'_r, \quad (2.21a)$$

$$s_6 = \tan \phi'_b \cos(\alpha/2) + \sin(\alpha/2), \quad (2.21b)$$

$$s_7 = \tan \phi'_b \sin(\alpha/2). \quad (2.21c)$$

The effective interaction force between the two wedges is now found from Equation (2.20):

$$N'_{\text{int}} = \left( \frac{1}{s_5} \right) \left( c'_r AB' s_6 + P_{\text{wint}} s_7 + (P_{w2} - P_{wfy} - W_2) \tan \phi'_b + \frac{d(M_2 v)}{dt} \right). \quad (2.22)$$

A single motion equation may be found now if the expressions of  $N'_{\text{int}}$  from Equations (2.12) and (2.22) are made equal. Rearranging terms, the following equation of motion is derived:

$$W_1 s_1 s_5 + (W_2 - P_{w2} + P_{wfy}) \tan \phi'_b s_2 + c'_r AB' (s_3 s_5 - s_2 s_6) - P_{\text{wint}} (s_4 s_5 + s_7 s_2) + P_{w1} \tan \phi'_b s_5 = s_5 \frac{d(M_1 v)}{dt} + s_2 \frac{d(M_2 v)}{dt}. \quad (2.23)$$

In order to simplify the notation, Equation (2.23) can be rewritten introducing new trigonometric coefficients  $t_i$ :

$$W_1 t_1 + (W_2 - P_{w2} + P_{wfy}) t_2 + c'_r AB' t_3 - P_{\text{wint}} t_4 + P_{w1} t_5 = s_5 \frac{d(M_1 v)}{dt} + s_2 \frac{d(M_2 v)}{dt} \quad (2.24)$$

where

$$t_1 = s_1 s_5, \quad (2.25a)$$

$$t_2 = \tan \phi'_b s_2, \quad (2.25b)$$

$$t_3 = s_3 s_5 - s_2 s_6, \quad (2.25c)$$

$$t_4 = s_4 s_5 + s_7 s_2, \quad (2.25d)$$

$$t_5 = \tan \phi'_b s_5. \quad (2.25e)$$

Under strict static equilibrium conditions, ( $d(M_1v)/dt = d(M_2v)/dt = 0$ ), Equation (2.24) could provide, for instance, the value of the apparent effective cohesion along shearing plane AB, in terms of the friction angle on AB,  $\phi'_r$ , wedge weights, pore pressure forces on their boundaries, and geometrical factors:

$$c'_r = \frac{-W_1t_1 - (W_2 - P_{w2} + P_{wf_y})t_2 + P_{wint}t_4 - P_{wl}t_5}{AB't_3}. \quad (2.26)$$

The water pressure forces entering the above equations are easily found as follows

$$P_{wf_y} = \frac{h_w^2 \gamma_w}{2 \tan \delta}, \quad (2.27a)$$

$$P_{w2} = (L_1 + L_2 + s)h_w \gamma_w, \quad (2.27b)$$

$$P_{wl} = \frac{h_w^2 \gamma_w}{2 \sin \alpha}, \quad (2.27c)$$

$$P_{wint} = \frac{h_w^2 \gamma_w}{2 \cos(\alpha/2)}. \quad (2.27d)$$

Initial ( $s = 0$ ) wedge volumes, in view of Figures 2.19 and 2.20, are given by

$$V_{10} = \frac{L_0 H_1}{2 \cos \alpha}, \quad (2.28a)$$

$$V_{20} = \frac{L_1 + L_2 + L_3}{2} H_1, \quad (2.28b)$$

which allows the calculation of wedge weights.

#### 2.6.4 Static equilibrium at failure

Cross-sections 2 and 5 (Fig. 2.14) are characterized by the geometrical parameters given in Table 2.1. The upper wedges of Sections 2 and 5 have similar volumes. However, the lower wedge of Section 2 has a significantly lower volume than Section 5. Therefore, Section 5 is more stable than Section 2, for a common set of strength parameters. Conditions for static equilibrium of these two sections will be first examined with the help of the set of relationships derived in the previous section. Since it has been argued that the residual friction at the basal sliding surface is a parameter known with sufficient certainty, the condition of stability may be used only to determine the strength parameters on shear plane AB. In fact, only combinations of the pair ( $c'_r$ ;  $\phi'_r$ ) may be found, since only one condition is available: the condition of static equilibrium at the initiation of failure (Eq.

(2.26)).

This is a nonlinear equation relating  $c'_r$  and  $\phi'_r$ , which has been plotted in Figure 2.21 for Sections 2 and 5, assuming  $\phi'_b$  equal to  $12^\circ$  and a rock specific weight of  $23.5 \text{ kN/m}^3$ .

**Table 2.1** Geometrical parameters of Cross-sections 2 and 5.

	$H_0$ (m)	$H_1$ (m)	$L_0$ (m)	$L_1$ (m)	$L_2$ (m)	$\alpha$ ( $^\circ$ )	$\delta$ ( $^\circ$ )	$V_1$ ( $\text{m}^3/\text{m}$ )	$V_2$ ( $\text{m}^3/\text{m}$ )
Section 2	580	245	750	190	260	37.7	43.3	116142	68149
Section 5	510	260	700	240	320	36	39.1	112590	93000

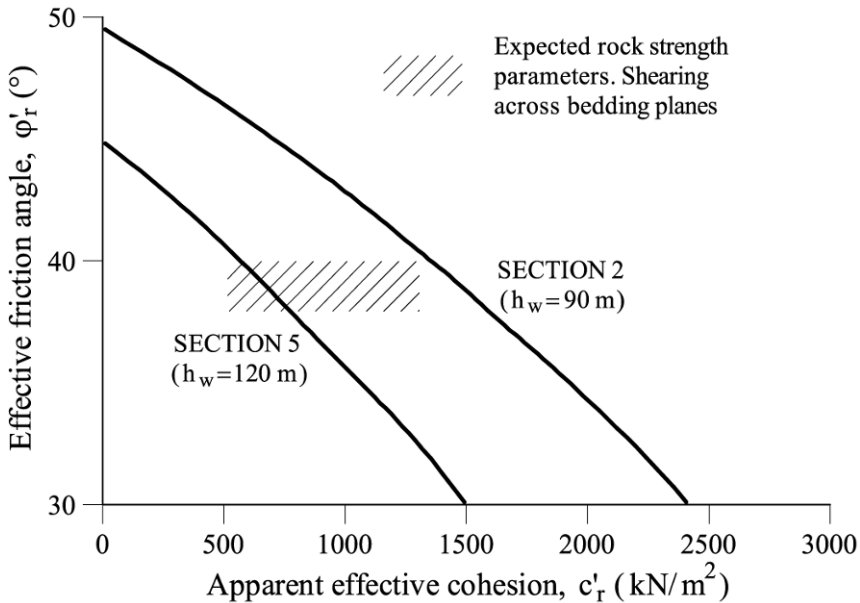
Forces  $P_w$  (Eq. (2.27)), which provide the effect of water pressures on both wedges, should correspond to failure conditions. Since a horizontal water level has been assumed and the preceding rain was shown to have a non-negligible effect (see Fig. 2.13), all water pressure influence will be associated with the water level height above the lower horizontal sliding surface,  $h_w$ . The plot in Figure 2.13 provides the estimation of the equivalent value of  $h_w$ , i.e.: the reservoir water level, in the absence of rain in the preceding 30-day period, which explains the failure. This height corresponds approximately to the elevation 710 m and, therefore, in Section 5 (see Figs. 2.8 or 2.14) it implies a value  $h_w = 120 \text{ m}$ . This reservoir elevation corresponds, in Section 2, to a water height of  $h_w = 90 \text{ m}$  (the failure surface daylights at a higher elevation at Section 2; see Figs. 2.8 and 2.14). The  $(c'_r; \phi'_r)$  values plotted in Figure 2.21 correspond to these two water elevations over the lower horizontal sliding plane.

Section 2 is “more demanding” in terms of required rock strength simply because of the relative weight of upper and lower wedges. This situation is reflected in the higher strength values required for the equilibrium calculated for Section 2 (Fig. 2.21). It is interesting to check that the  $(c'_r; \phi'_r)$  combinations in Figure 2.21 are in fairly good agreement with the strength expected in rock sheared across bedding planes, discussed in 2.6.3. Since the variability of  $\phi'_r$  values is small compared with the expected variation of cohesive intercepts ( $c'_r$ ), a band of expected  $(c'_r; \phi'_r)$  pairs, centered around  $\phi'_r = 38^\circ\text{--}40^\circ$  has been plotted in Figure 2.21 as a reasonable estimation of the rock strength along shear plane AB.

If Section 5 is taken as a representative cross-section of the slide, the following combinations lead to strict equilibrium of Vaiont slide:  $(c'_r = 762.3 \text{ kPa}; \phi'_r = 38^\circ)$ ;  $(c'_r = 564.0 \text{ kPa}; \phi'_r = 40^\circ)$ .

It is also interesting to examine the interaction forces between the two blocks and how they change as a function of the available friction on the basal sliding plane. Equations (2.12) and (2.22), for zero acceleration, provide this force for the two wedges. If Section 5 is selected for the analysis, the variation of  $N'_{\text{int}}$  with the base friction angle for two pairs of values  $(c'_r; \phi'_r)$  is given in Figure 2.22. It was already stated that equilibrium is achieved if the interaction force  $N'_{\text{int}}$  between

the upper and lower wedges is forced to have a common value. This condition also implies that the shear force,  $Q_{\text{int}}$ , and therefore the total interaction force are equal.



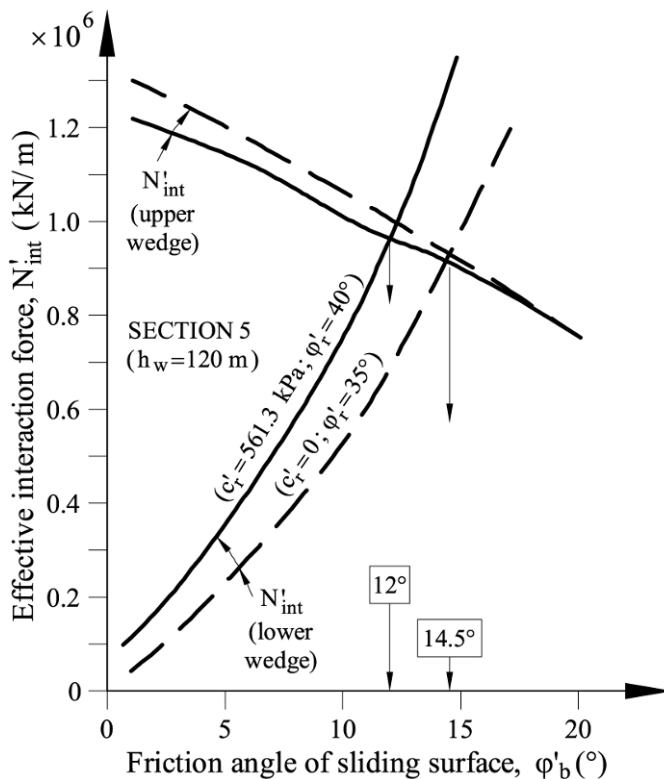
**Figure 2.21** Strength parameters across shearing plane AB for equilibrium. Sections 2 and 5. Basal friction:  $\phi'_b = 12^\circ$ .

Figure 2.22 shows how the stabilizing  $N'_{\text{int}}$  force offered by the lower wedge increases fast as the friction at the sliding surface,  $\phi'_b$ , increases. On the other hand, the unbalanced  $N'_{\text{int}}$  force required for the equilibrium of the upper wedge decreases as  $\phi'_b$  increases, but at a slower rate. Overall equilibrium is achieved when both forces are equal. For strength parameters  $c'_r = 564.0 \text{ kN/m}^2$  and  $\phi'_r = 40^\circ$  equilibrium is achieved for  $\phi'_b = 12^\circ$ , a result which has already been found. If the strength along the shear plane AB is reduced to  $c'_r = 0 \text{ kN/m}^2$  and  $\phi'_r = 35^\circ$ ,  $\phi'_b$  has to increase to  $14.7^\circ$ , to reach equilibrium.

So far, equilibrium conditions have been used to find the mobilized strength parameters at failure. The condition of failure, when it is properly identified, which means, in particular, that slide geometry and pore water pressure distribution are known, is a procedure to find strength parameters or, better, a relationship among the strength parameters involved in the model selected to perform stability calculations. This procedure, illustrated above, is often described as a “back-analysis” of the failure.

In addition, one may be interested in knowing the safety factor for conditions other than failure. For instance, in the case of Vaiont, it makes sense to ask for the

safety conditions of the slope before dam impoundment or at some particular elevation of the reservoir surface. These questions are addressed in the next section.



**Figure 2.22** Effective interaction force,  $N'_{int}$  between upper and lower wedges. Section 5 of Vaiont slide.

### 2.6.5 Safety factors

In limit equilibrium methods (the analyses developed before belong to this class of methods) the safety factor is defined as the ratio between the available shear strength of the soil or rock and the shear stress necessary for strict equilibrium. Shear strength and shear stress are calculated on the failure surface. The model of two interacting wedges developed in 2.6.3 and 2.6.4 includes two failure surfaces: the “basal” surface that bounds the landslide and an internal shear surface (AB), which makes it kinematically possible. The nature of both surfaces is quite different: the former is located in a high plasticity clay in residual conditions, whereas the internal shear surface crosses sedimentary planes, distorts a competent rock and exhibits significant strength. However, it is quite possible that shear displacements will decrease to some extent the shear strength of this shear plane. For a particular situation of the slide (for instance, under natural conditions



before dam construction), the two shearing surfaces will most probably not mobilize their shear strength in equal proportions. Likewise, if a change in external conditions takes place (reservoir impoundment, or rainfall), the available strength will not be mobilized at the same time among the two surfaces because the shear stiffness of the shearing surfaces and, indeed, of the whole rock mass, will also play a significant role.

Since the problem is complicated, let us accept, to initiate the discussion, that two different safety factors,  $F_b$  and  $F_r$ , are appropriate for the two surfaces. Then, the mobilized strength parameters will be defined as follows:

$$\tan \phi'_{b\text{mob}} = \tan \phi'_b / F_b, \quad (2.29a)$$

$$\tan \phi'_{r\text{mob}} = \tan \phi'_r / F_r, \quad (2.29b)$$

$$c'_{r\text{mob}} = c'_r / F_r. \quad (2.29c)$$

A relevant question is to ask for the safety factor,  $F_r$ , of the Vaiont slide at the beginning of impoundment (i.e.,  $h_w = 0$ ), in the hypothesis that the mobilized stress at the basal sliding surface remained at residual conditions,  $\phi'_b = 12^\circ$ , (i.e.,  $F_b = 1$ ). It is also of interest to know how  $F_r$  would change, still under  $F_b = 1$ , if the slide moves forward following the mechanism described in Figure 2.15.

Alternatively, one may wish to maintain the classic approach and to find a unique and global safety factor,  $F$ , for the two situations mentioned, ( $F = F_b = F_r$ ). The two possibilities will be examined here.

For Cross-section 5, it was found that the following set of strength parameters:  $\phi'_b = 12^\circ$ ;  $c'_r = 762.2$  kPa;  $\phi'_r = 38^\circ$  leads to failure when  $h_w = 120$  m. If these parameters are accepted as true strength parameters, then the equilibrium equations given in 2.6.3 are also valid, for conditions other than failure, if the reduced strength parameters (2.29a,b,c) are used instead of the true strength values (which are now assumed to be known). In other words, equilibrium conditions are now satisfied for the mobilized stresses prevailing at the shear surfaces. In fact, mobilized shear stresses are defined as those which satisfy equilibrium conditions. Therefore, in view of Equations (2.29), the overall equilibrium equation can be used to find the safety factor. However, the equilibrium equation will now be a function of  $F_b$  and  $F_r$  and therefore only **one** safety factor may be determined – either  $F$  if it is accepted that  $F = F_b = F_r$ , or  $F_r$  if  $F_b$  is fixed, for instance at  $F_b = 1$ , or any other alternative. This situation is similar to the already discussed determination of strength parameters at failure.

If the mobilized strength parameters (Eqs. (2.29a,b,c)) are substituted into the equilibrium Equation (2.26), the following expression is obtained.

$$\frac{c'_r}{F_r} = \frac{-W_1 t_1(F_r, F_b) - (W_2 - P_{w2} + P_{wf}) t_2(F_r, F_b) + P_{wint} t_4(F_r, F_b) - P_{wl} t_5(F_r, F_b)}{AB' t_3(F_r, F_b)}, \quad (2.30)$$

where the dependence of the  $t_i$  expressions on the safety factors has been explicitly indicated in the Appendix 2.1. If Equation (2.30) is developed, it turns out to be a second-order algebraic equation for  $F_r$  (Eq. (A2.4) in the Appendix 2.1), which may be solved if  $F_b$  is assumed to be known. Details of the solution of Equation (2.30) are relegated to Appendix 2.1.

The safety factor  $F_r$  of Section 5 of the Vaiont slide was obtained for:

- Water pressure conditions prior to failure. As discussed before, pore water-pressure effects are integrated into the variable  $h_w$ , the reservoir level over the lower horizontal sliding plane.
- The changing geometry, as the slide moves forward and the water level maintains maximum elevation,  $h_w = 120$  m. This is a purely static analysis performed on different geometries of the slide as it moves forward. The dynamics of the motion will be introduced in the next section and it will be discussed in more detail in Chapter 5.
- The effect of  $h_w$  on safety factor  $F_r$ , when  $F_b = 1$ , is plotted in Figure 2.23 (dashed line). The calculated value for  $h_w = 0$  ( $F_r = 1.2$ ) is not particularly high and it indicates that the mobilized strength in the rock mass before any impounding was quite substantial in order to maintain the slope in equilibrium.

The analysis of the changing geometry, shown in Figure 2.15, leads to the safety factor  $F_r$  plotted in Figure 2.24 (dashed line). The increase of  $F_r$ , again for  $F_b = 1$ , becomes more pronounced as slide displacement increases. The high values calculated for  $s = 150$  m ( $F_r = 5$ ), indicate that the mobilized resistance across shear plane AB is no longer necessary to maintain equilibrium. In fact, beyond  $s = 179$  m, the residual friction angle at the main sliding surface is able to maintain the slope in equilibrium without any contribution from the sheared rock mass across the shear plane AB.

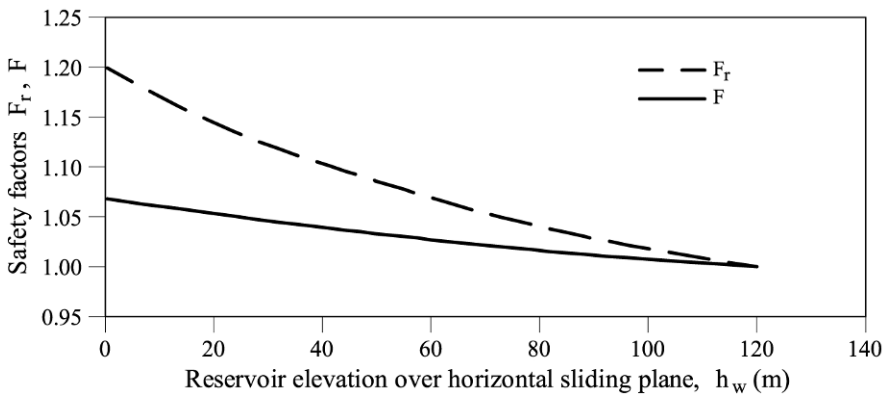


**Figure 2.23** Section 5. Evolution of safety factor,  $F_r$  (if  $F_b = 1$ ; see text) and global safety factor,  $F$ , when the water level increases in the reservoir.

Let us now consider the determination of a unique global safety factor  $F$ . The condition  $F = F_b = F_r$  has to be introduced in Equation (2.30). The equilibrium

Equation (2.30) now becomes a fourth-order polynomial for the unknown  $F$ . A simple numerical procedure to solve the equation is described in Appendix 2.2.

Calculated global safety factors, with the help of Equation (A2.10), were plotted in Figures 2.23 and 2.24 (continuous line). Computed values of  $F$  are now significantly lower than the previously reported values of  $F_r$ .

One advantage of global safety factors is that geotechnical engineers have developed, over the years, a scale of numerical values that helps them to approximate the risk of failure.  $F$  values of 1.5 and above are generally regarded as indicators of a low risk of failure of slopes. A safety factor of 1.2 is probably close to the minimum that many would regard as an acceptable situation. Since different calculation procedures often result in changes in safety factor of  $\pm 0.1$  for a given slope stability problem, a safety factor of 1.1 conveys a clear message of risk.

However, one should distinguish between design situations and, on the other hand, the problem of analyzing an existing slide and its remedial measures. In the second case, the evidence of field instability, if properly interpreted, provides a robust reference value ( $F = 1$  for failure conditions) which acts as a validation benchmark for any method of stability analysis. Then, calculated changes of safety factor over the reference situation ( $F = 1$ ) are significantly more reliable than a pure predicting exercise based, for instance, on strength parameters determined in the laboratory or on estimated pore water pressures derived from flow calculations.

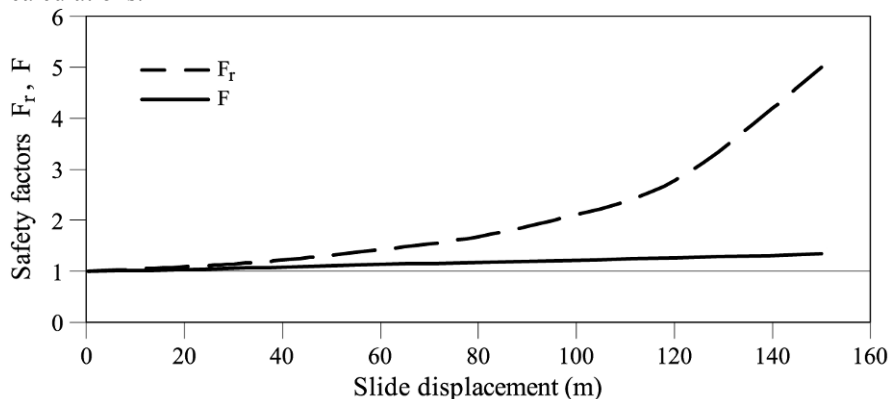


**Figure 2.24** Section 5;  $h_w = 120$  m. Evolution of safety factor,  $F_r$  (if  $F_b = 1$ ; see text) and global safety factor,  $F$ , with slide displacement.

Vaiont obviously belongs to the second category. Nevertheless, the global safety factors calculated for changing water levels within a very large range (0 to 120 m of water column) (Fig. 2.23) look particularly low ( $F$  decreases from  $F = 1.07$  for  $h_w = 0$  m to  $F = 1$  for  $h_w = 120$  m). This is certainly a consequence of the very large size of the landslide but it also points out that the presence of the reservoir implied a relatively minor change in the safety of the slope, always within the perspective of risk associated with the classical definition of a global

safety factor. Moreover, this result is also an indirect indication that in very large landslides, feasible remedial measures are expected to lead to relatively low increments of safety factor.

Figure 2.24 shows that the motion of the slide results in geometries with an increasing global safety factor. Given the preceding comments, changes are far from being negligible. In fact, displacements of 40, 100, and 150 m imply  $F$  values of 1.08, 1.22, and 1.36 respectively. (Interestingly, very similar changes were computed with the much simpler two-block model, Fig. 2.17b.) The increasing sophistication of the model did not change this basic result.

The relevant question in this case, already stated when discussing the two block model results, is to ask for the reasons for the accelerated motion of a landslide which seemed to move in a direction of increased stability. This aspect is essentially the subject of Chapter 5 but some additional discussion is offered in the next section.

### 2.6.6 Landslide run out

Equilibrium conditions, when inertia terms are included, results in the motion Equation (2.24). This equation, taking into account Equation (2.6) has the following form:

$$\frac{dv}{dt} = \frac{W_1 t_1 + (W_2 - P_{w2} + P_{wf_y}) t_2 + c'_r AB' t_3 - P_{wint} t_4 + P_{w1} t_5 - s_5 \frac{dM_1}{dt} - s_2 \frac{dM_2}{dt}}{(s_5 + s_2)}, \quad (2.31)$$

where time derivatives of  $M_1$  and  $M_2$  are known (Eq. (2.15)) and they depend on displacement and velocity. The weights ( $W_1$  and  $W_2$ ) and the length  $AB'$  also depend on the displacement. Therefore, Equation (2.31) can be written as

$$a = \frac{dv}{dt} = f(s, v). \quad (2.32)$$

At any given time of the motion, slide acceleration ( $a = dv/dt$ ) is a function of slide displacement,  $s$  and velocity,  $v$ . Function  $f$  also includes information on geometry, specific weights, water pressures, and strength parameters. Finding a close-form solution for  $v(t)$  is a hard task but the structure of (2.32) invites to develop a simple numerical algorithm of integration. If the following discrete approximation is adopted, the value of the acceleration and the velocity at time  $(t + 1)$  can be calculated as

$$a_{i+1} = \left( \frac{dv}{dt} \right)_i = \frac{v_{i+1} - v_i}{t_{i+1} - t_i} = f(s_i, v_i), \quad (2.33a)$$

$$v_{i+1} = v_i + f(s_i, v_i)(t_{i+1} - t_i), \quad (2.33b)$$

which are functions of known values evaluated in time  $t$ . In this way, an explicit time integration procedure is developed. Reducing  $\Delta t = t_{i+1} - t_i$  leads to

progressively more accurate results.

Displacements can be estimated from the following expression

$$v_i = \left( \frac{ds}{dt} \right)_i = \frac{s_{i+1} - s_i}{t_{i+1} - t_i} \quad (2.34a)$$

and therefore:

$$s_{i+1} = s_i + v_i (t_{i+1} - t_i). \quad (2.34b)$$

In view of the nature of the problem and the simplicity of the underlying mechanical model, it is probably not justified in this case to look for more sophisticated integration procedures. The integration algorithm was implemented in an Excel calculation sheet. Note that masses, weights and the length  $AB'$  should be updated at each time interval since they depend on the displacement.

It was argued in Section (2.6.3), when developing the model of two interacting wedges, that the effective rock cohesive intercept,  $c'_r$ , would be degraded during shear along plane AB. Since relative shear displacements along AB are controlled by displacement  $s$ , a simple degradation model will make  $c'_r$  dependent on  $s$ . For instance,

$$c'_r = c'_{r0} \exp(-\Gamma s), \quad (2.35)$$

where  $\Gamma$  is a constant (units:  $\text{length}^{-1}$ ) that controls the rate of rock degradation and  $c'_{r0}$  is the initial cohesion intercept ( $c'_{r0} = 768.35 \text{ kPa}$  for Cross-section 5, if  $\phi'_r = 38^\circ$ , and accepting that  $\phi'_b = 12^\circ$ ). Expression (2.35) was also included in the motion equation in order to explore the effect of loss of shear strength on the dynamics of the motion. It is not reasonable, however, to expect a strong degradation of cohesion along  $AB'$  and the reason is that the rock mass “crosses” the plane  $AB'$  during the motion and therefore new – more or less undisturbed – rock is continuously sheared across AB.

Consider the following scenario: in a situation of strict equilibrium (reservoir elevation at  $h_w = 120 \text{ m}$  in Cross-section 5) the water level is increased by a small amount (say  $h_w = 121 \text{ m}$ ), and it is maintained as constant thereafter. It is desirable to find the motion of the slide until a new situation of equilibrium is reached. Since the slide improves its static stability conditions as  $s$  increases – a result from the previous section – it should be expected that the slide will come to rest after some displacement.

The solution to this problem (which is the solution of Eq. (2.31) plotted as a relationship between the run out ( $s$ ) and the velocity on the moving mass ( $v$ )) is shown in Figure 2.25 for no degradation of the rock strength ( $\Gamma = 0$ ). The result shows that the slide stops after a displacement of  $0.30 \text{ m}$  and reaches a maximum velocity of  $1.7 \text{ cm/s}$ . If the water level is increased to  $h_w = 124 \text{ m}$  and to  $h_w = 130 \text{ m}$ , maximum displacements and velocities increase as shown in Figure 2.25, but the calculated values are far from the actual behaviour of the landslide, which reached velocities estimated in  $30 \text{ m/s}$ , more than two orders of magnitude higher

than the maximum values found in this calculation.

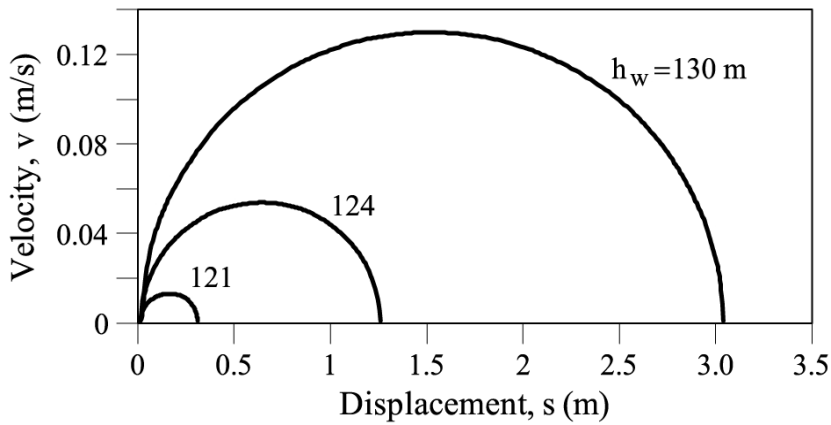


**Figure 2.25** Cross-section 5. Calculated run outs and slide velocities for  $h_w = 121$ , 124, and 130 m. No rock strength degradation ( $\Gamma = 0$ ).

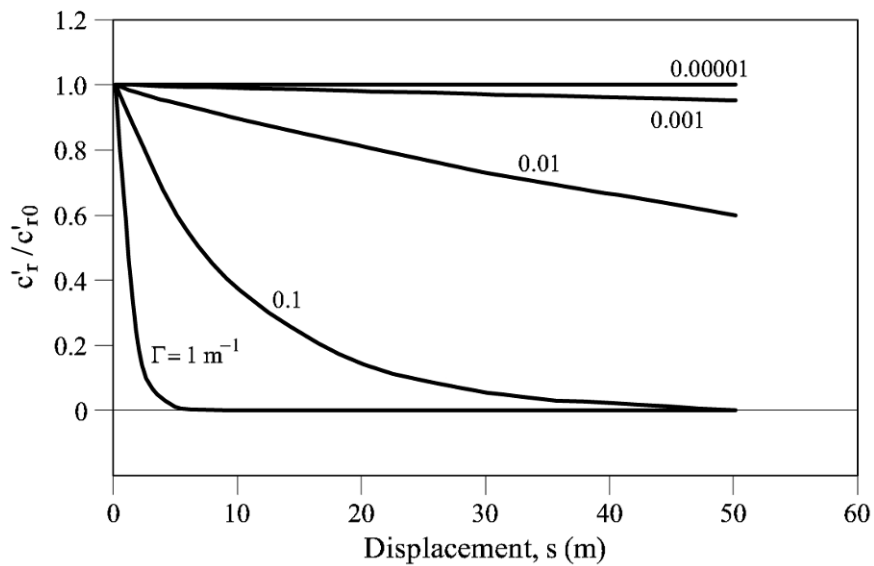


**Figure 2.26** Assumed loss of effective cohesive strength parameter across shearing plane AB with slide displacement, for several values of parameter  $\Gamma$ .

The situation changes if some rock strength degradation is introduced into the analysis.

Figure 2.26 is a plot of Equation (2.35) for a few values of the degradation parameter  $\Gamma$ . It will be used as a reference for the results of run-out calculations.

Now the scenario is to start the slide motion by increasing the water level (to

$h_w = 121$  m) and to accept a certain degradation of the rock during the motion. The calculated response of the slide, again in terms of velocity vs. displacement, is shown in Figures 2.27 and 2.28. A moderate degradation of the effective strength parameter of the rock ( $\Gamma = 0.01 \text{ m}^{-1}$ , Fig. 2.27) has a limited effect on the maximum sliding velocity and on the travelled distance. However, if the degradation of rock effective cohesion is more rapid ( $\Gamma = 0.1 \text{ m}^{-1}$  and  $\Gamma = 1 \text{ m}^{-1}$ ; Fig. 2.28), the slide is able to travel long distances (60–70 m), although the maximum velocity does not increase beyond 3 m/s (16.2 km/h) even if a very rapid and complete destruction of the rock effective cohesion is imposed (for  $\Gamma = 1$ , see Fig. 2.28). Under the more realistic assumption of moderate rock degradation,  $\Gamma \leq 1 \text{ m}^{-1}$ , the maximum slide velocity is quite small.

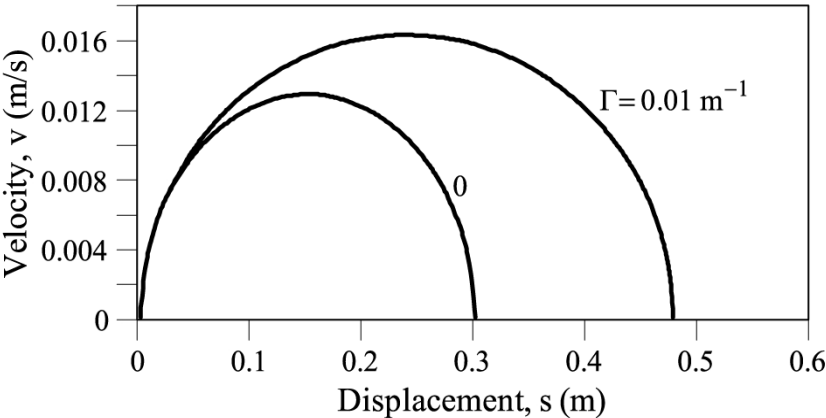


**Figure 2.27** Cross-section 5. Calculated run outs and slide velocities for  $h_w = 121$  m. Effect of rock strength degradation ( $\Gamma = 0$  and  $\Gamma = 0.01 \text{ m}^{-1}$ ).

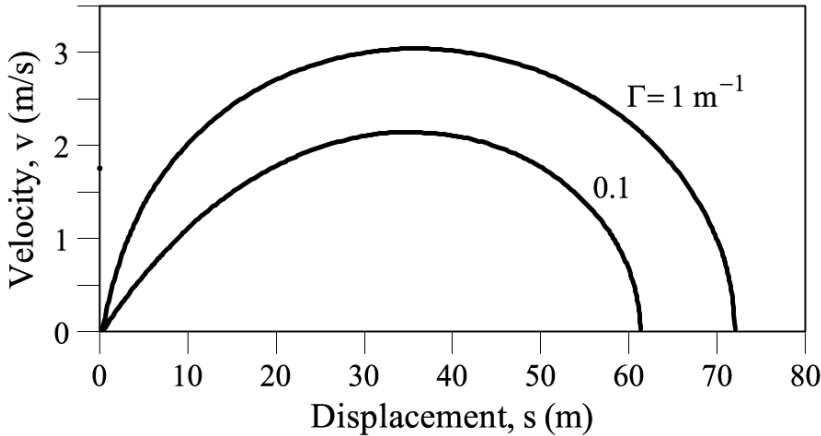


**Figure 2.28** Cross-section 5. Calculated run outs and slide velocities for  $h_w = 121$  m. Effect of rock strength degradation ( $\Gamma = 0.1$  and  $\Gamma = 1 \text{ m}^{-1}$ ).

In all the cases analyzed, the mechanism leading to stopping the landslide motion is the change in geometry of the slide as it moves downwards.

The dynamic analysis developed here maintains, unanswered, the key question of the extremely high velocities reached by the slide. However, it indicates that a loss of internal rock strength, associated with the slide motion itself, is a potential mechanism to accelerate the slide.

## 2.7 Discussion

The investigations on the past history of the landslide by Semenza (2001), synthesized in Figure 2.7, and the work of Hendron and Patton (1987) highlight two fundamental aspects: Vaiont was a case of a slide reactivation and the sliding surface was located in fairly continuous layers of high plasticity clay. Taken together, the implication is that the basal sliding surface could not offer, against a new reactivation of the slide (essentially induced by an increase in pore water pressures in the lower massive passive wedge of the slide), an effective friction angle larger than, say,  $10\text{--}12^\circ$ . A good proportion of published back-analysis of Vaiont, which use conventional methods of limit equilibrium to find the actual friction angle prevailing at the sliding surface at the time of failure is not consistent with Vaiont past history. In fact, published back-analyses lead to friction angles in the range  $18\text{--}28^\circ$  (the simple two-block model of 2.6.2 is an example in this regard). Vaiont exhibits a safety factor significantly lower than one if a friction angle of  $10\text{--}12^\circ$  (and zero effective cohesion) is used in any of the currently available methods of slices. How to address this inconsistency?

Hendron and Patton (1987) argue that the side friction on the eastern edge of the slide provided the necessary resisting force to ensure equilibrium (however, some limited information on the direction of the displacements on this border, plotted in Fig. 2.2, tends to indicate that the moving mass was detaching from the stable rock massif). The alternative explanation developed here is that the kinematics of the motion, even in a two-dimensional cross-section, requires the relative shearing between the two large rock wedges defining the slide. Leonards (1987) also pointed out that the motion of the slide required such a rock shearing between the upper and the lower sliding blocks. The estimated shearing strength parameters across the common shearing plane are in reasonable agreement with the expected mass strength of cretaceous marls and limestones of Vaiont.

The acceleration of the motion during the catastrophic failure escapes the capabilities of the models presented here. A loss of strength is expected when rock masses are sheared, due to its inherent brittleness and the complex development of strains within the moving mass. “Progressive failure” is the term often used to describe these phenomena. The end result is a loss of the cohesive components of strength. Such a loss, when imposed on the strength available on the interacting shearing plane between the upper and lower wedges, results in an acceleration of the slide, which is unable to explain the high velocities reached by the landslide, even if a rapid and complete loss of rock cohesion is imposed (Section 2.6.6). Therefore, it becomes important to look for additional explanations for the apparent loss of strength experienced by the actual slide. If the mechanism of side



friction proposed by Hendron and Patton (1985) is accepted as additional resisting phenomena, the need for a convincing mechanism for strength loss is even more pronounced. The discussion of this fundamental matter will continue in Chapter 5.

## 2.8 Lessons Learned

### 2.8.1 Slide reactivation

Ancient slides are rightly regarded as trouble-makers when they are affected by engineering works. Past sliding activity is responsible for the reduction of the strength available along “dormant” sliding surfaces to minimum values (“residual” strengths). In addition, if sliding surfaces are associated with high plasticity clays, the residual friction angles are particularly low. Typically, ancient slides in these circumstances maintain a low safety factor, which may be rapidly exhausted by engineering works. Vaiont is a good example.

### 2.8.2 Submerging the slide toe

Submerging the toe of slopes usually leads to a reduction of stability. The safety factor decreases as the water level increases. The reduction is first pronounced but, eventually, the negative effect associated with the reduction of effective normal stresses on the sliding surface is compensated by the beneficial hydrostatic forces acting against the exposed slope<sup>(1)</sup>.

The safety factor reaches a minimum value for some intermediate water level and then increases again to reach values close to the initial safety factor of the “aerated” slope. The precise evolution of the safety factor when the reservoir water level increases depends also on the particular distribution of pore water pressures inside the slope, but a fundamental aspect of this problem is the geometry of both the slope and the sliding surface. Three examples are shown in Figure 2.29 to illustrate these comments. All of them were solved with a commercial slope stability program for soil slopes using the Morgenstern – Price method (Morgenstern and Price, 1965). In all cases the distribution of pore pressures inside the slide follows a horizontal water table. The first case (Fig. 2.29a) reproduces the geometry of Vaiont, Section 5. A uniform friction angle,  $\phi' = 12^\circ$  (and zero effective cohesion) is assumed. The safety factor reaches a minimum for  $h_w/H = 0.5$ . A similar result is obtained if the lower sliding surface is inclined (Fig. 2.29b; now  $\phi' = 15^\circ$ ). However, for a conventional slope (the upstream slope of an earthdam) and a critical circular failure surface, the

---

<sup>(1)</sup> An alternative explanation can be given in terms of submerged weights. When a lower part of the slope is flooded, its effective weight becomes the submerged weight (roughly equal to one half of the saturated total weight). Therefore, normal effective stresses on the sliding plane are reduced. But the (effective) weight also reduces. This weight has often a positive stabilizing effect when it is close to the toe. Therefore, reducing it also decreases the safety factor. But, as the water level increases, the upper parts of the slope, which contribute with unstabilizing weight, also reduce its effect and the calculated safety factor will increase again beyond some critical water level.

minimum is reached for  $h_w/H = 0.3$ .

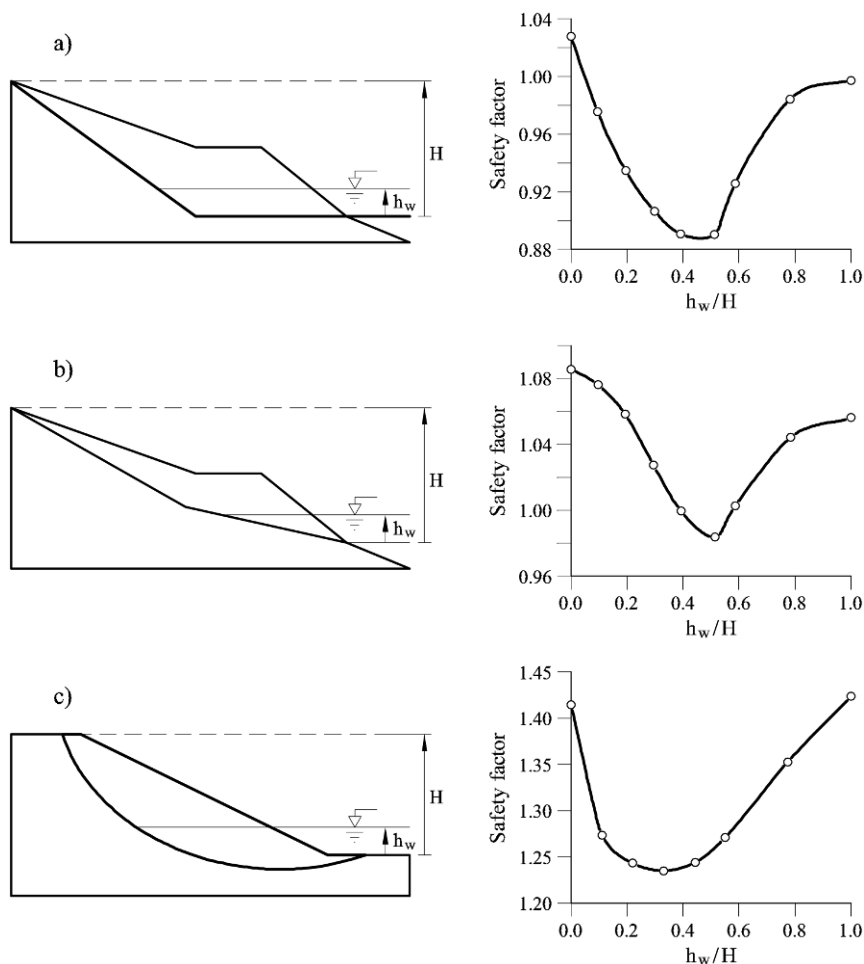


**Figure 2.29** Evolution of safety factor (Morgenstern – Price method) when the water level in the reservoir increases.  $h_w$ : water level above the elevation of the exit point of the sliding surface.  $H$ : maximum value of  $h_w$ , when the entire slope is submerged. Case (a) geometry of Vaiont and ( $c' = 0$ ;  $\varphi' = 12^\circ$ ); Case (b): geometry modified from Case (a) and ( $c' = 0$ ;  $\varphi' = 15^\circ$ ); Case (c): conventional slope and circular failure surface ( $c' = 0$ ;  $\varphi' = 30^\circ$ ).

The geometry of Vaiont is especially sensitive to the submergence of the toe, because the large toe passive wedge offers an ever decreasing resisting force when submerged. This is further illustrated in Figure 2.30, which shows a calculation of the global safety factor of Section 5, following the procedure described in 2.6.5. The height of the dam prevented  $h_w$  values higher than 145 m, approximately, in Section 5. Unfortunately, Vaiont slide never entered in a zone of increasing stability.

In conclusion, flooding slope toes is not good practice but it is an unavoidable situation in many circumstances, notably in valley slopes affected by dam reservoirs. If the initial safety factor is low (this was the case of Vaiont) flooding the toe implies trouble ahead. Note also that it takes a substantial water level elevation before the trend for lower safety, as the water level increases, is reversed.

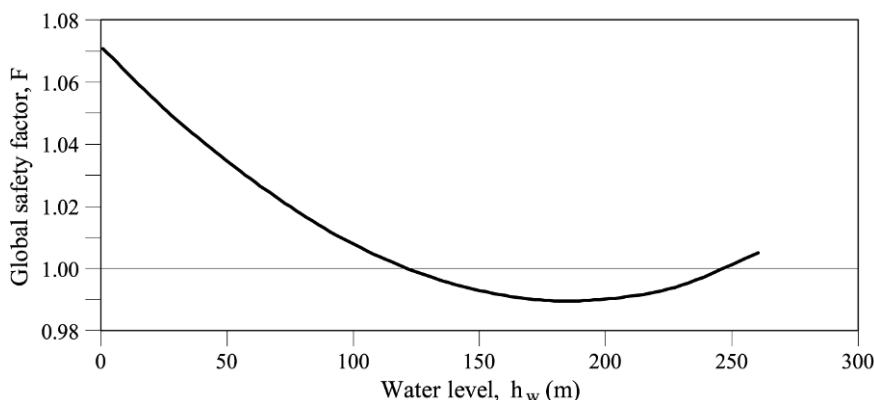


**Figure 2.30** Variation of global safety factor with height of water above the horizontal basal plane. Two-wedge model. Section 5 of Vaiont.

### 2.8.3 Interpretation of field data

Interpretation of sliding risk was essentially made on the basis of reservoir elevation and surface displacements. There was also information on rainfall and on the levels of four piezometers. The “piezometers” were in fact open tubes which did not reach the level of the sliding surface and only provided average water pressures prevailing along their length. In addition, no direct information of the position of the failure surface and, in particular, on the type of material being sheared was available.

Identification of a landslide for the purposes of estimating its evolution and of defining any remedial measure requires information of a few key variables. Ideally, these key variables should also be used in the formulation of a mechanical model of the motion. In the case of Vaiont, early knowledge of the following data concerning the basal failure surface: geometry, pore water pressure, type of material, and drained strength parameters would have been fundamental to build a conceptual and mechanical model for the slide. This is a first step in understanding the problem, not only for Vaiont, but for any landslide. In the case of Vaiont, the observation that the slide velocity decreased when the reservoir level was reduced, irrespective of the absolute level of the water, provided a reservoir filling criterion which, finally led to the failure. In some sense, an “observational method”<sup>(2)</sup> was

<sup>(2)</sup> The observational method, described by Peck (1969), requires the following ingredients: a) direct observation of a key variable or property describing the essential nature of the problem; b) a proper conceptual, analytical or computational model able to provide an

applied: the conceptual model was essentially given by the preceding observation, illustrated in Figure 2.12. The key variables to be interpreted were the displacement rates of surface markers and the reservoir level. The action in mind, in case of excessive displacement rate, was to reduce the water level in the reservoir. It was accepted, despite this strategy, that a full slide was a likely event and that the expected height of the generated wave was even estimated by model studies. However, the conceptual model was not based on any mechanical analysis of the slide. In addition, the reservoir level did not necessarily provide the actual pore pressures on the failure surface and the remedial plans were too simple and weakly connected with the complex mechanisms taking place within the slide.

It should be borne in mind that these comments are made more than 50 years after the first investigations started in Vaiont. Their purpose is to learn from the case, not to criticize the involved individuals who had to work with the techniques and rules of practice available at that time.

Even today, managing a very large landslide is a daunting task. We are well equipped to extract field data (pore water pressures, absolute deformations, “in-situ” tests) in the first tens of meters of soil and rock. Going beyond 200 m requires sophisticated, not easily available, and time-consuming efforts. In addition, a very large landslide requires a vast site investigation. It is not a matter of only a few borings. Therefore, the difficulties to handle large landslides continue to be present and the words of Carlo Semenza, the dam designer, remain as a vivid testimony of the formidable challenge he was facing: “[...] *things are probably bigger than us and there are no adequate practical measures [...]* After so many fortunate works and so many structures [...] *I am in front of a thing which due to its dimensions seems to escape from our hands [...]*”, (in a letter written in April 1961, quoted by Nonveiller, 1987; the full letter in Italian was published in Semenza, 2001).

#### 2.8.4 Computational procedures

Most of the limiting equilibrium procedures commonly available to the geotechnical profession (methods of slices) do not include an internal shearing in the moving mass, which is described by strength parameters other than the parameters operating on the external bounding failure surface. Moreover, none of them may handle processes of stress redistribution induced by progressive failure mechanisms. In addition, they have no capability to approximate the initial stress state. Continuum models (finite elements) may reproduce better the stress state derived from a known history of slope development but modelling progressive failure is still a research subject with very little impact on current practice. It has to be accepted that, 47 years after the disaster, static methods to estimate the stability conditions of the Vaiont landslide still suffer from important limitations. To aggravate things, the dynamic behaviour of the slide is still being discussed

---

estimation of the risk, in a general sense, for some threshold values of the key variable(s) and c) a plan, defined in advance, to act in a specified manner when threshold values are exceeded.

and investigated. From a practical point of view, there are no reliable criteria to estimate the dynamic reaction of an impending landslide in the case of failure. More will be said in Chapter 5 on this aspect

One has to accept for the time being, by a simple comparison with Vaiont, that large landslides exhibiting symptoms of instability, sliding on (high plasticity?) clay levels and subjected to a definite reduction of stability conditions, may develop unexpected sliding velocities.

### 2.8.5 Could it have been avoided?

This has been a subject of much debate (see Leonards, 1987). It is probably fair to say that an improved knowledge of the field situation – based on a more comprehensive set of sensors, a detailed geology, and the strength properties of the sliding surface – and even a better conceptual and mechanical model of the slide would not have provided reliable criteria to stop the motion. Large engineering works also convey important pressures to be completed as planned. If this was the case of the Vaiont dam, there was probably not a reasonable procedure to avoid the slide. In fact, this risk was accepted by the designers, as mentioned before. There were also (abandoned) attempts to drain the failure surface by means of a drainage tunnel. Its potential effect remains unclear especially because the reservoir level marked an unavoidable minimum interstitial water pressure, which was already very high. Even if the operating water level of the reservoir was substantially reduced (more than 100 m), there remains the risk that an exceptional rainfall event (see Fig. 2.13) could have brought the water pressures to critical values. Perhaps a combination of a significant (no less than 100 m) reduction of the maximum reservoir level and an expensive tunnel-based drainage scheme of the failure surface could have achieved a sufficiently low risk of failure.

### Appendix 2.1 Safety Factor $F_r$ . Static Equilibrium

Equation (2.30) provides the condition of equilibrium of the entire slide in terms of mobilized strength parameters given in Equations (2.29). Coefficients  $t_i$  in Equation (2.30) are now written in more detail:

$$t_1 = s_1(F_b)s_5(F_b, F_r), \quad (\text{A2.1a})$$

$$t_2 = \frac{\tan \phi'_b}{F_b} s_2(F_b, F_r), \quad (\text{A2.1b})$$

$$t_3 = s_3(F_b)s_5(F_b, F_r) - s_2(F_b)s_6(F_b, F_r), \quad (\text{A2.1c})$$

$$t_4 = s_4(F_b)s_5(F_b, F_r) + s_7(F_b)s_2(F_b, F_r), \quad (\text{A2.1d})$$

$$t_5 = \frac{\tan \varphi'_b}{F_b} s_5(F_b, F_r), \quad (\text{A2.1e})$$

where

$$s_1(F_b) = \sin \alpha - \cos \alpha \frac{\tan \varphi'_b}{F_b}, \quad (\text{A2.2a})$$

$$\begin{aligned} s_2(F_b, F_r) &= \sin(\alpha/2) \frac{\tan \varphi'_b}{F_b} - \cos(\alpha/2) \frac{\tan \varphi'_r}{F_r} \frac{\tan \varphi'_b}{F_b} + \\ &\cos(\alpha/2) + \sin(\alpha/2) \frac{\tan \varphi'_r}{F_r} = s_{a2}(F_b) + s_{b2}(F_b)/F_r, \end{aligned} \quad (\text{A2.2b})$$

$$s_3(F_b) = \cos(\alpha/2) \frac{\tan \varphi'_b}{F_b} - \sin(\alpha/2), \quad (\text{A2.2c})$$

$$s_4(F_b) = \sin(\alpha/2) \frac{\tan \varphi'_b}{F_b} + \cos(\alpha/2), \quad (\text{A2.2d})$$

$$\begin{aligned} s_5(F_b, F_r) &= \cos(\alpha/2) - \sin(\alpha/2) \frac{\tan \varphi'_b}{F_b} - \cos(\alpha/2) \frac{\tan \varphi'_r}{F_r} \frac{\tan \varphi'_b}{F_b} - \\ &\sin(\alpha/2) \frac{\tan \varphi'_r}{F_r} = s_{a5}(F_b) + s_{b5}(F_b)/F_r, \end{aligned} \quad (\text{A2.2e})$$

$$s_6(F_b) = \cos(\alpha/2) \frac{\tan \varphi'_b}{F_b} + \sin(\alpha/2), \quad (\text{A2.2f})$$

$$s_7(F_b) = \sin(\alpha/2) \frac{\tan \varphi'_b}{F_b}, \quad (\text{A2.2g})$$

where

$$s_{a2}(F_b) = \sin(\alpha/2) \frac{\tan \varphi'_b}{F_b} + \cos(\alpha/2), \quad (\text{A2.3a})$$

$$s_{b2}(F_b) = \tan \varphi'_r \left( \sin(\alpha/2) - \cos(\alpha/2) \frac{\tan \varphi'_b}{F_b} \right), \quad (\text{A2.3b})$$

$$s_{a5}(F_b) = \cos(\alpha/2) - \sin(\alpha/2) \frac{\tan \phi'_b}{F_b}, \quad (\text{A2.3c})$$

$$s_{b5}(F_b) = \tan \phi'_r \left( -\sin(\alpha/2) - \cos(\alpha/2) \frac{\tan \phi'_b}{F_b} \right). \quad (\text{A2.3d})$$

If Equations (A2.1) to (A2.3) are substituted into Equation (2.30), the following algebraic equation for  $F_r$  is obtained:

$$aF_r^2 + bF_r + c = 0, \quad (\text{A2.4})$$

where

$$a = As_{a5} - Cs_{a2}, \quad (\text{A2.5a})$$

$$b = As_{b5} + Bs_{a5} - Cs_{b2} - Ds_{a2}, \quad (\text{A2.5b})$$

$$c = Bs_{b5} - Ds_{b2}, \quad (\text{A2.5c})$$

and

$$A = W_1 s_1(F_b) - P_{\text{wint}} s_4(F_b) + P_{\text{w1}} \frac{\tan \phi'_b}{F_b}, \quad (\text{A2.6a})$$

$$B = c'_r m' s_3(F_b), \quad (\text{A2.6b})$$

$$C = P_{\text{wint}} s_7(F_b) + \frac{\tan \phi'_b}{F_b} (P_{\text{wf}_y} - P_{\text{w2}} + W_2), \quad (\text{A2.6c})$$

$$D = c'_r m' s_6(F_b). \quad (\text{A2.6d})$$

The valid root of Equation (A2.4) is

$$F_r = \left( -b + \sqrt{b^2 - 4ac} \right) / 2a. \quad (\text{A2.7})$$

## Appendix 2.2 Global Safety Factor $F$

Equation (A2.7), when  $F = F_r = F_b$ , is, in fact, the static equilibrium equation. Therefore, the value of  $F$  should satisfy

$$G(F) = F - \left( -b + \sqrt{b^2 - 4ac} \right) / 2a = 0, \quad (\text{A2.8})$$

where the terms  $a$ ,  $b$ ,  $c$  in (A2.8) should now be calculated for  $F$ .

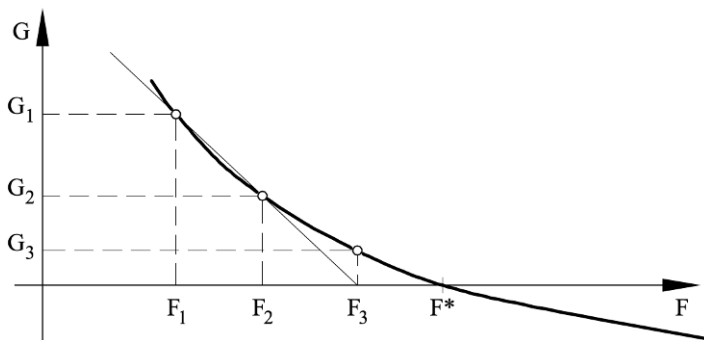


**Figure A2.1** Numerical determination of global safety factor,  $F$ .

Consider in Figure A2.1 the function  $G(F)$ . The solution sought is marked as  $F^*$ . Consider now two  $F$  values ( $F_1$  and  $F_2$ ) and the corresponding  $G$  values given by (A2.8). The straight line through  $(F_1, G_1)$  and  $(F_2, G_2)$  intersects the  $F$  axis at  $F_3$ , given by

$$F_3 = F_2 - \frac{G(F_2)(F_1 - F_2)}{G(F_1) - G(F_2)}, \quad (\text{A2.9})$$

which could be generalized, as  $F_i$  approaches  $F^*$

$$F_i = F_{i-1} - \frac{G(F_{i-1})(F_{i-2} - F_{i-1})}{G(F_{i-2}) - G(F_{i-1})}. \quad (\text{A2.10})$$

Equation (A2.10) provides a recurrent expression to find the target  $F^*$ . The success of the procedure depends on the shape of function  $G$  around  $F^*$ . The upwards concave shape illustrated in Figure A2.1 is the actual shape of (A2.8) in the vicinity of the solution (which, actually, is quite close to the critical value  $F = 1$ ). For all the global safety factors calculated the two initial values of  $F_i$  to initiate the calculation through Equation (A2.10) were  $F_1 = 1$  and  $F_2 = 1.01$ .

## References

- Barton, N. (2007) *Rock Quality, Seismic Velocity, Attenuation and Anisotropy*. Taylor and Francis. London.
- Belloni, L.G. and Stefani, R. (1987) The Vajont slide: Instrumentation – Past experience and the modern approach. *Engineering Geology* 24, 445–474.
- Broili, L. (1967) New knowledge on the geomorphology of the Vaiont Slide slip surface. *Rock Mechanics and Engineering Geology* 5, 38–88.
- Hendron, A.J. and Patton, F.D. (1985) The Vaiont slide, a geotechnical analysis based on new geologic observations of the failure surface. *Technical Report GL-85-5*. Department of the Army US Army Corps of Engineers, Washington, DC.
- Hendron, A.J. and Patton, F.D. (1987) The Vaiont slide. A geotechnical analysis



- based on new geologic observations of the failure surface. *Engineering Geology* 24, 475–491.
- Hoek, E. (2007) Practical Rock Engineering  
<http://www.rocksience.com/hoek/PracticalRockEngineering.asp>
- Jaeger, C. (1965) The Vaiont rockslide. Part I. *Water Power*. March, 110–111.
- Jaeger, C. (1965) The Vaiont rockslide. Part II. *Water Power*. April, 142–144.
- Kenney, T.C. (1967) Stability of the Vajont valley slope, discussion of a paper by L. Müller (1964) on the rock slide in the Vajont valley. *Rock Mechanics and Engineering Geology* 5, 10–16.
- Leonards, G.A. (1987) Overview and personal commentary. *Engineering Geology* 24, 577–612.
- Lupini, J.F., Skinner, A.E. and Vaughan, P.R. (1981) The drained residual strength of cohesive soils. *Géotechnique* 31 (2), 181–213.
- Menzel, V. (1966) Mechanics of landslides with non-circular slip surfaces with special reference to the Vaiont Slide. *Géotechnique* 19 (4), 329–337.
- Morgenstern, N.R. and Price, V.E. (1965) The analysis of the stability of general slip surfaces. *Géotechnique* 15, 79–93.
- Müller, L. (1964) The rock slide in the Vajont Valley. *Rock Mechanics and Engineering Geology* 2, 148–212.
- Nonveiller, E. (1967) Shear strength of bedded and jointed rock of landslides with noncircular surfaces with special reference to Vajont slides. *Proceedings of the Geotechnical Conference*. Oslo, Norway. Norwegian Geotechnical Institute. 1, 289–294.
- Nonveiller, E. (1987) The Vajont reservoir slope failure. *Engineering Geology* 24, 493–512.
- Peck, R.B. (1969) Advantages and limitations of the observational method in applied soil mechanics. Ninth Rankine Lecture. *Géotechnique* 19 (2), 171–187.
- Semenza, E. (2001) *La Storia del Vaiont Raccontata del Geologo che ha Scoperto la Frana. Tecomproject*. Editore Multimediale. Ferrara.
- Semenza, E. and Ghirotti, M. (2000) History of the 1963 Vaiont slide: the importance of geological factors. *Bulletin of Engineering Geology and the Environment* 59, 87–97.
- Skempton, A.W. (1966) Bedding-plane slip, residual strength and the Vaiont landslide. *Correspondence to Géotechnique* 16 (2), 82–84.
- Tika, Th.E. and Hutchinson, J.N. (1999) Ring shear tests on soil from the Vaiont slide slip surface. *Géotechnique* 49 (1), 59–74.
- Valdés Díaz-Caneja, J.M. (1964) Meditaciones sobre la Catástrofe del Vaiont. *Boletín n° 20*. Servicio Geológico. Ministerio de Obras Públicas. Madrid.

Geomechanics of Failures. Advanced Topics

Alonso, E.E.; Pinyol, N.M.; Puzrin, A.M.

2010, VIII, 277 p., Hardcover

ISBN: 978-90-481-3537-0